OPECAL

D12:ATBD CLOUD SCREENING

TECHNICAL NOTE

	Name	Company	Date	Signature
Prepared by :	B. Berthelot	Magellium	30/01/2015	
Checked by :				
Approved by :	B. Berthelot	Magellium	30/01/2015	

Document reference :	OPECAL-TN-019-MAG
Issue.Revision :	2.0
Date :	30/01/2015
Client :	ESRIN
Ref., Tender :	AO/1-7043/11/F/MOS

EN-MAG-MOD.DT-GEN-034-v1.3

Distribution list

	Name	Company	N. copies
Addresses :	M. Bouvet G. Ottavianelli	ESA/ESTEC ESA/ESRIN	1
Internal copy :	Customer file Project Manager Development team	Magellium Magellium Magellium	1 (digital) 1 (digital) 1 (digital)

Document Change Record

Iss.	Rev.	Date	Reason	Comments
1	0	27/06/2013	Creation of the document	
2	0	30/01/2015	Update	

Table of contents

List of the Tables

List of the Figures

1 Introduction of the technical note

1.1 Objectives of the document

The purpose of this study is to improve the cloud screening methodologies implemented into DIMITRI software.

1.2 Related documents

1.2.1 Applicable documents

Table 1: List of applicable documents

Id.	Ref.	Description
AD1	QA4EO-QAEO-GEN-DQK-001/7, Version 4.0	QA4EO Guidelines (seven documents) http://qa4eo.org/

1.2.2 Reference documents

Table 2: List of reference documents

Id.	Ref.
RD. 1.	Bouvet M. , Ramoino F., Radiometric intercomparison of AATSR, MERIS, and Aqua MODIS over Dome Concordia (Antarctica), Can. J. Remote Sensing, Vol. 36, No. 5, pp. 464–473, 2010. http://pubs.casi.ca/loi/cjrs
RD. 2.	DIMITRI Software User Manual ftp://ftp.estec.esa.int/pub/gsp/anonymous/Earth_Observation_Multi-mission_Phase-E2_Operational_Calibration/DIMITRI_SUM.pdf
RD. 3.	DIMITRI Software Design Document ftp://ftp.estec.esa.int/pub/gsp/anonymous/Earth_Observation_Multi-mission_Phase-E2_Operational_Calibration/DIMITRI_SDD.pdf
RD. 4.	Statement of Word GSP activity 'Towards the Intercalibration of EO Medium Resolution Multi-Spectral Imagers' ftp://ftp.estec.esa.int/pub/gsp/anonymous/Earth_Observation_Multi-mission_Phase-E2_Operational_Calibration/SoW_GSP_TowardsTheIntercomparisonOfEOMediumResolutionMultiSpectralImagers.pdf
RD. 5.	Hagolle et Al., Results of POLDER in-flight Calibration, IEEE Transactions on Geoscience and Remote Sensing, May 1999, Volume 37, Number 03 [p. 1550]. http://ieeexplore.ieee.org/xpl/RecentIssue.jsp?punumber=36
RD. 6.	Vermote, E., R. Santer, P.Y. Deschamps and M. Herman, In-flight Calibration of

	Large Field-of-View Sensors at Short Wavelengths using Rayleigh Scattering, Int. Journal of Remote Sensing, 13, No 18, 1992. http://www.tandf.co.uk/journals/tres
RD. 7.	Smith D., Poulsen C., Latter B.: Calibration Status of the AATSR Reflectance Channels, MERIS AATSR workshop 2008 proceedings. http://earth.esa.int/meris_aatsr_2008/

1.2.3 Bibliography

- Ackerman, S. A., K. I. Strabala, W. P. Menzel, R. A. Frey, C. C.Moeller, and L. E. Gumley, 1998: Discriminating clear-sky from clouds with MODIS. J. Geophys. Res., 103 (D24), 32 141–32 157.

1.2.4 Acronyms

6SV	Second Simulation of a Satellite Signal in the Solar Spectrum, Vector
AATSR	Advanced Along Track Scanning Radiometer
ADEOS	Advanced Earth Observation Satellite
AERONET	AErosol RObotic NETwork
ASTR	Along Track Scanning Radiometer
AVHRR	Advanced Very High Resolution Radiometer
BRDF	Bidirectional Reflectance Distribution Function
Cal/Val	CALibration and VALidation
CEOS	Committee on Earth Observation Satellites
CNES	Centre National d’Etudes Spatiales
DIMITRI	Database for Imaging Multispectral Instruments and Tools for Radiometric Intercomparison
ENVISAT	ENVIronment SATellite
EO	Earth Observation
ESA	European Space Agency
ETM	Enhanced Thematic Mapper
EUMETSAT	European Organisation for the Exploitation of Meteorological Satellites
GSICS	Global Space-based Inter-calibration System
IVOS	Infrared and Visible Optical Sensors
LandNet	Land Network
MERIS	Medium Resolution Imaging Spectrometer
Meteosat	Meteorological Satellite
MetOp	Meteorological Operational
MISR	Multi-angle Imaging SpectroRadiometer
MODIS	Moderate Resolution Imaging Spectroradiometer
NASA	National Aeronautics and Space Administration
NOAA	National Oceanic and Atmospheric Administration
OLCI	Ocean and Land Color Instrument

PARASOL	Polarization & Anisotropy of Reflectances for Atmospheric Sciences coupled with Observations from a Lidar
POLDER	POLarization and Directionality of the Earth's Reflectances
RTM	Radiative Transfer Model
SADE	Structure d'Accueil de Données d'Etalonnage
SLSTR	Sea and Land Surface Temperature Radiometer
SWIR	Short Wave Infra-Red
TOA	Top Of Atmosphere
VGT	VEGETATION
VIS	VISible
VITO	Vision on Technology (Flemish Institute of Technological Research)

2 Introduction

The main objective of the document is to describe the algorithmic improvements performed on the cloud screening methodologies already implemented into DIMITRI software. The software processes images acquired by ATSR-2, AATSR, MODIS/Aqua, MERIS, PARASOL, and VEGETATION instruments.

The algorithms are dedicated to flag the data which are acquired on clear sky condition in order to select a clean dataset used for the sensor calibration.

This document is structured as follows:

- Section 3 :Overview of the algorithms implemented and reference results
- Section 4 :Improvement of the algorithms and results

3 Algorithm overview

3.1 Objectives

The objectives of this section are to assess the cloud detection over DIMITRI calibration sites for the 6 following sensors.

- MODIS/Aqua ;
- PARASOL ;
- MERIS ;
- AATSR ;
- VEGETATION ;
- ATSR-2.

3.2 Background

A mandatory requirement for all EO systems is the stability of sensor performance in order to guarantee consistency in data over time, and comparable performance between sensors. Test sites have a pseudo-invariant reflectance behaviour. Any changes can be traced back to data anomalies, or changes in sensor calibration/sensor performance. Before attributing the change to a change of sensor calibration, several procedures are set. Cloud screening is one of the data preprocessing steps. In DIMITRI software, three methods have been implemented to flag the data used in radiometric calibration monitoring:

1. Landsat ACCA for ATSR2, AATSR and MODIS-Aqua;
2. Globcarbon-MERIS for MERIS, POLDER-3;
3. VGT operational cloud screening for VEGETATION.

These methodologies are efficient because they combine information coming from the visible/near Infra-red/short infrared and thermal part of the solar spectrum (if available). However their adaptation to other sensors with different spectral and spatial characteristics is a difficult step that might have degraded their capabilities.

Cloud misdetection is one of the factors which alter the accuracy of the radiometric calibration.

The functioning of the algorithms is identical whatever the sensors. The pixel classification mask is filled by using different filters comparing index, ratio, band combinations to thresholds at each step of the algorithm (Figure 1: Cloud mask filling). All pixels classified as ambiguous, desert or snow at the end are reassigned as cloud or clear in a second step.

The four steps of the algorithms are:

- Step 1: Mask initialization;
- Step 2: At each test, the cloud mask is filled with a flag;
- Step 3: All flags except clear and cloud (see Table 3) are restored to clear and clouds depending on site type;
- Step 4: The cloud coverage is estimated by counting the number of cloudy pixels out to the total of the site.

The flags set during the processing are the following:

Table 3: Set of flags available for each method

Landsat ACCA	Globcarbon-MERIS	VGT operational
CLEAR_ID = 1 SNOW_ID = 2 AMBI_ID = 3 COLD_CLOUD_ID = 4 WARM_CLOUD_ID = 5 CLOUD_ID = 6	ICLEAR = 0 ICLOUD = 1 ISNOW = 2 IBRIGHT = 3	CLEAR_FLAG = 0 CLOUDY_FLAG = 1 SNOW_FLAG = 2

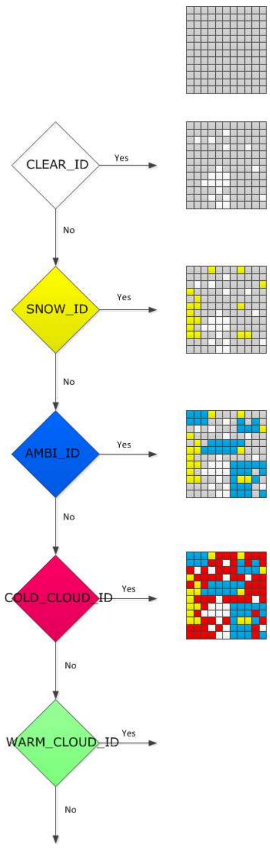

Figure 1: Cloud mask filling

The results of the cloud detection estimated using the version 2 of the software are used as reference results. They are provided for all sites and all sensors for the full time series of data provided in the database. However, these results are those obtained automatically by applying the algorithm. We must remind that the user might change the flag manually using the software if the detection is not good.

3.3 Inputs

3.3.1 Datasets

The datasets, including the version of the processing are reported in the next table.

Table 4: Reference of the products

Sensor	Dataset reference
MODIS	MYD021KM: MODIS/Aqua Calibrated Radiances 5-Min L1B Swath 1km (Collection 5)
MERIS	MERIS Level 1b Reduced resolution, Level 1B Reprocessing 2 and 3
PARASOL	Calibration 1
VEGETATION	VGT-P
ATSR-2	ATSR-2 data reprocessing 2008
AATSR	AATSR, 2^{nd} reprocessing

This following table summarised the channels used in the cloud detection.

Table 5: Channels used in cloud detection algorithms

Source	Landsat ACCA			Globcarbon-MERIS		VGT operational
Wave Centre	**AATSR**	**ATSR2**	**MODISA**	MERIS	PARASOL	VEGETATION
412			0	0		
443			1	1	0	0
470			15			
490			2	2	1	
510				3		
530			3			
555	0	0	4/16	4	2	
620				5		
665	1	1	5/6/20	6	3	1
681			7/8	7		
708				8		
750			9	9		
761				10	4	
765					5	
778				11		
830						2
860			21			
870	2	2	10	12	6	
885				13		
900			11	14	7	
935			12			
940			13			
1020					8	
1240			17			
1375			14			
1600	3	3	18			3
2130			19			
3700	4	4				
10850	5	5				
12000	6	6	22			

For MODIS sensor, the bands are ordered as there are in the products. 13 bands acquired at 1km, 6 bands acquired at 500m and resampled to 1km (MODIS bands 3 to 7), 2 bands acquired at 250m and resampled to 1km (MODIS bands 1 and 2).

3.3.2 Sites

The site location is reported in the following table.

Site name	Location	Illustration
Tuz Golu:	[38.80 N, 38.70 N, 33.25 E, 33.40 E]	
Uyuni salt lake	[-20.16 S, -20.00 S, -68.05 W, -67.45 W]	
Amazonian forest	[1 N, 1.33 N, -57 W, -56.5 W]	
Dome C	[-75.2 S, -75.0 S, 123.2 E,123.6 E]	
Libyan desert	[28.7 N, 29.0 N, 23.5 E,23.8 E]	

Site name	Location	Illustration
BOUSSOLE	[43.25 N, 43.45 N, 7.8 E,8.0 E]	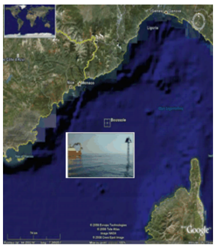
South Pacific Gyre	[-30.5 S, -31.0 S, -129.0 W, -129.5 W]	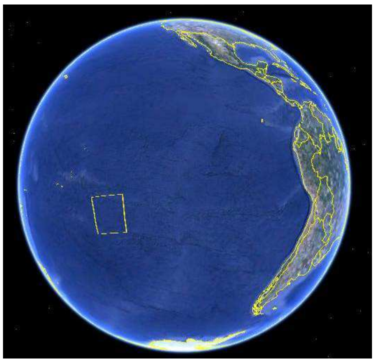
South Indian Ocean	[-30.0 S, -30.5.0 S, 80.0 E, 80.50 E]	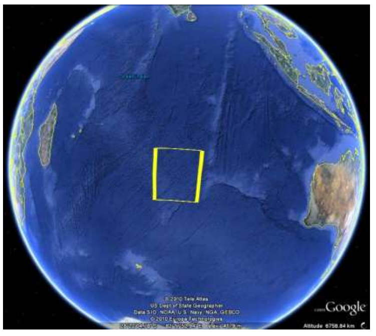

3.4 Reference results

3.4.1 Representation of the reference results

Outputs of the cloud screening (before manual correction) are reported for each site/each sensor using a figure representing the NIR TOA reflectances versus time for the full time series, where the mean level of cloudiness is represented for each acquisition by a color code varying between 0 and 1.

This view allows to detect easily the performance of the algorithms and focuses on adaptation or modifications of the algorithm in order to identify the source of errors and correct them if it is needed. A second step consists in analyzing the images of cloud mask versus the spectral information for a specific day/sensor to adjust more accurately the thresholds used in the algorithms.

3.4.2 MODIS

3.4.2.1 SIO

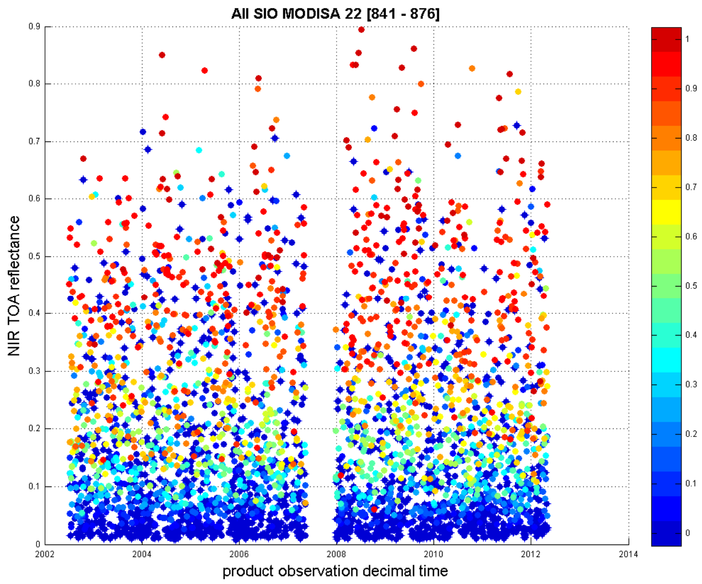

Figure 2: NIR TOA reflectance versus acquisition time. Cloud coverage level is indicated with colortable.

3.4.2.2 SPG

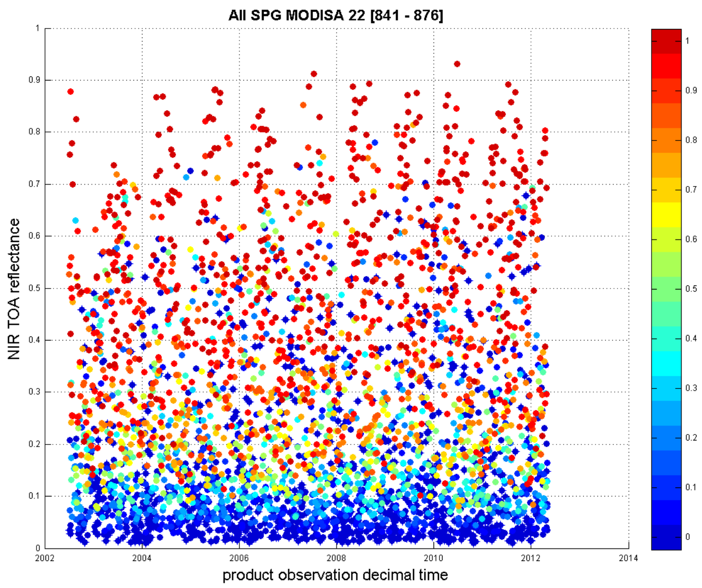

Figure 3: NIR TOA reflectance versus acquisition time. Cloud coverage level is indicated with colortable.

3.4.2.3 Boussole

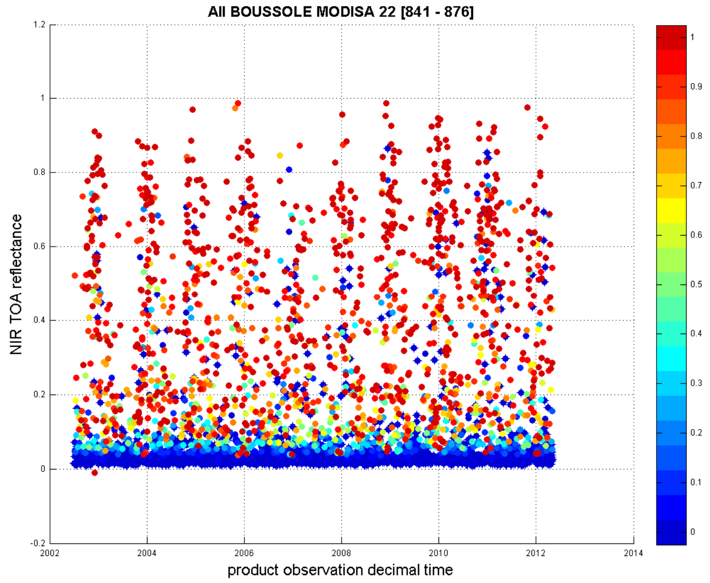

Figure 4: NIR TOA reflectance versus acquisition time. Cloud coverage level is indicated with colortable.

3.4.2.4 Amazon

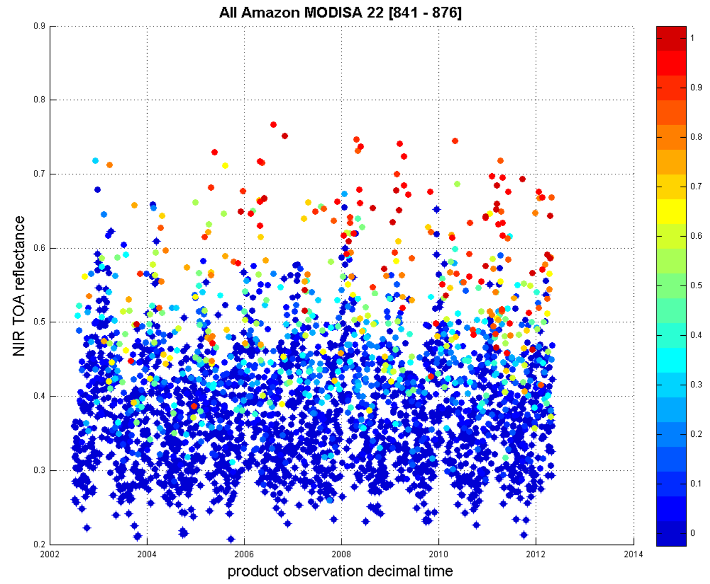

Figure 5: NIR TOA reflectance versus acquisition time. Cloud coverage level is indicated with colortable.

3.4.2.5 DomeC

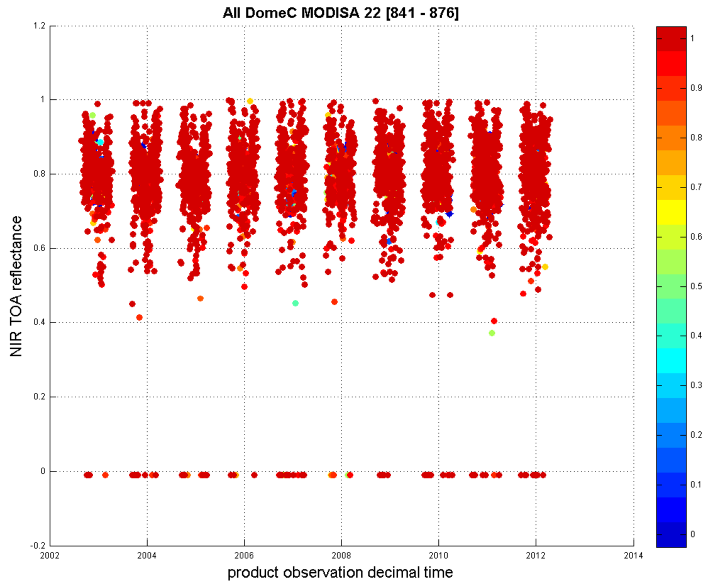

Figure 6: NIR TOA reflectance versus acquisition time. Cloud coverage level is indicated with colortable.

3.4.2.6 Uyuni

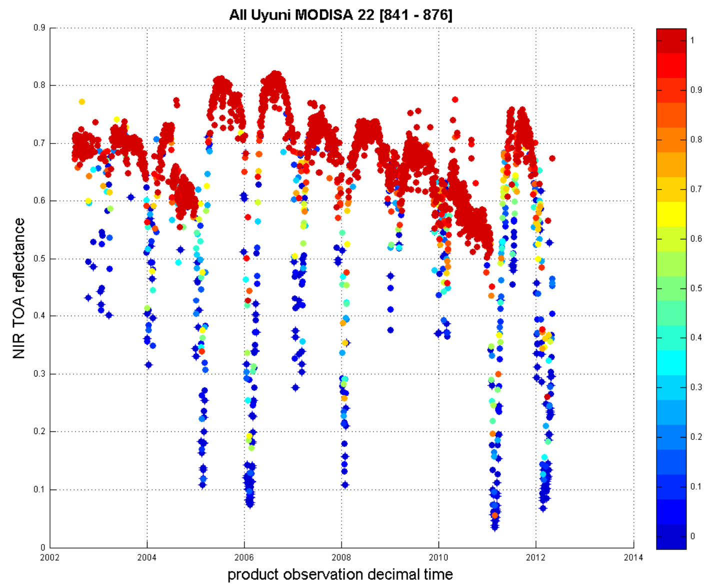

Figure 7: NIR TOA reflectance versus acquisition time. Cloud coverage level is indicated with colortable.

3.4.2.7 TuzGolu

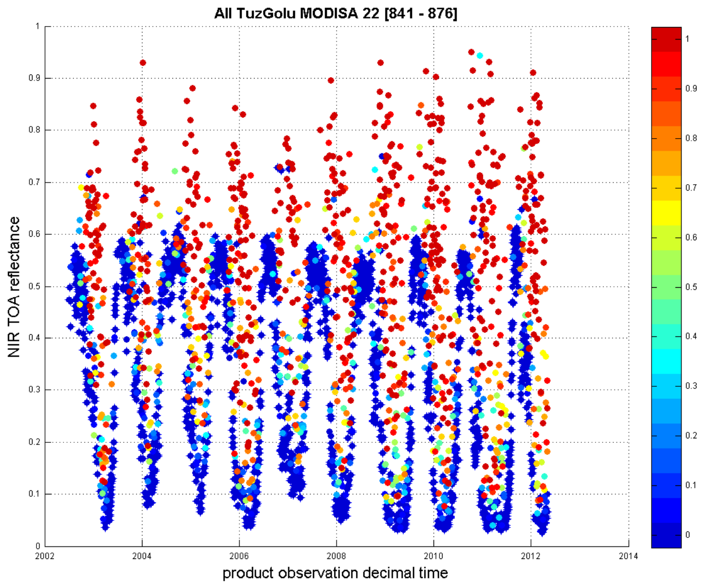

Figure 8: NIR TOA reflectance versus acquisition time. Cloud coverage level is indicated with colortable.

3.4.2.8 Libya4

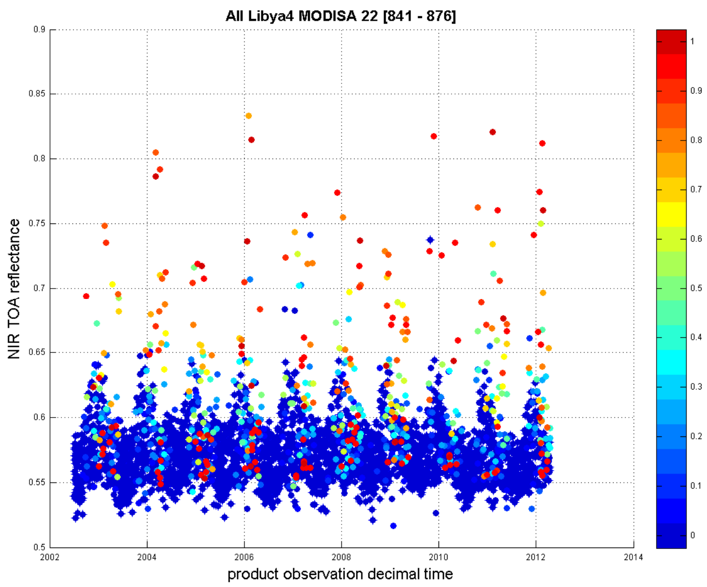

Figure 9: NIR TOA reflectance versus acquisition time. Cloud coverage level is indicated with colortable.

3.4.3 MERIS

3.4.3.1 SIO

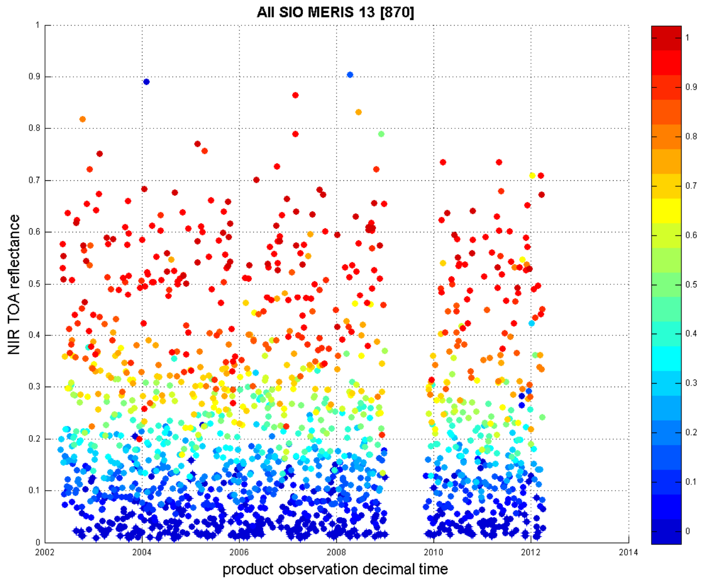

Figure 10: NIR TOA reflectance versus acquisition time. Cloud coverage level is indicated with colortable.

3.4.3.2 SPG

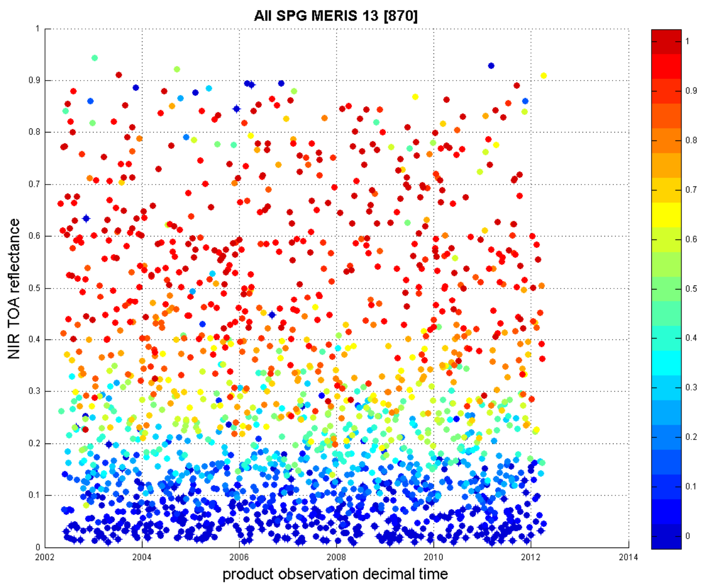

Figure 11: NIR TOA reflectance versus acquisition time. Cloud coverage level is indicated with colortable.

3.4.3.3 Boussole

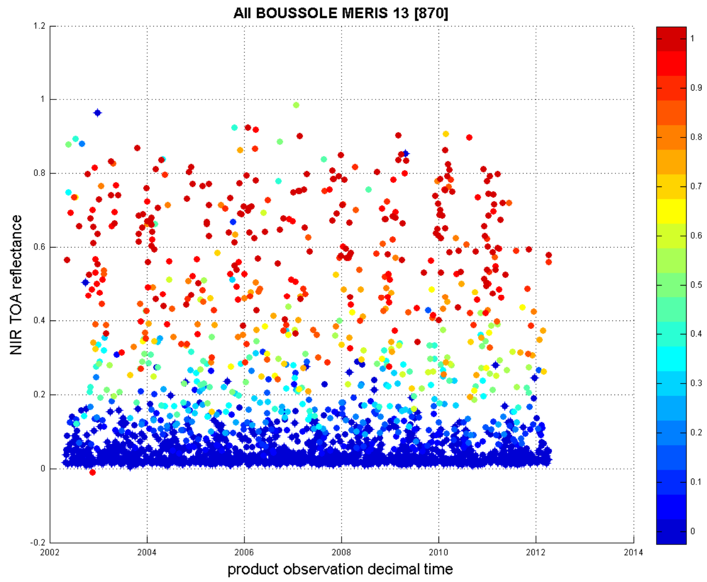

Figure 12: NIR TOA reflectance versus acquisition time. Cloud coverage level is indicated with colortable.

3.4.3.4 Amazon

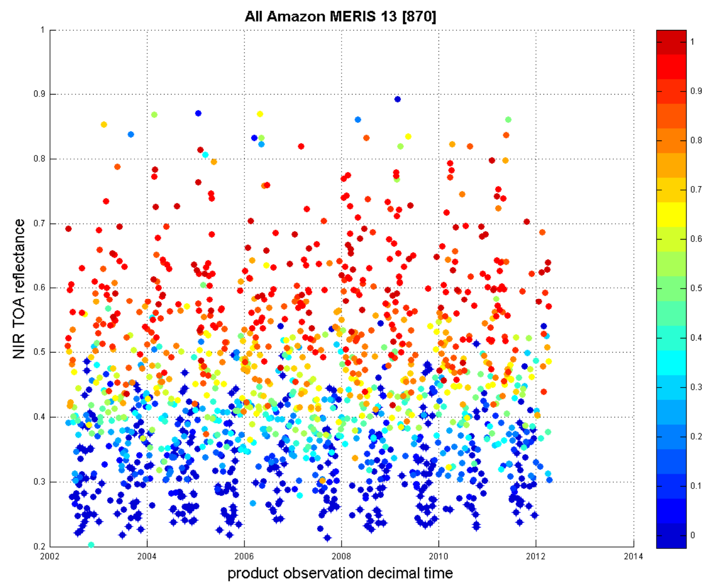

Figure 13: NIR TOA reflectance versus acquisition time. Cloud coverage level is indicated with colortable.

3.4.3.5 DomeC

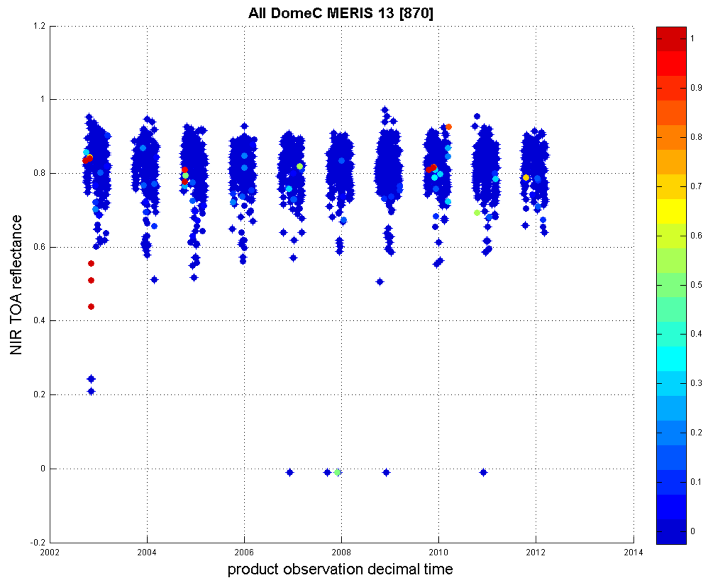

Figure 14: NIR TOA reflectance versus acquisition time. Cloud coverage level is indicated with colortable.

3.4.3.6 Uyuni

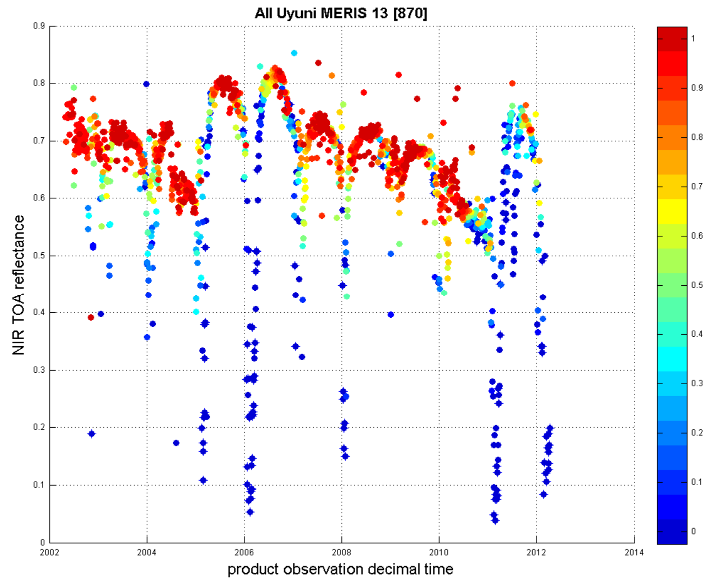

Figure 15: NIR TOA reflectance versus acquisition time. Cloud coverage level is indicated with colortable.

3.4.3.7 TuzGolu

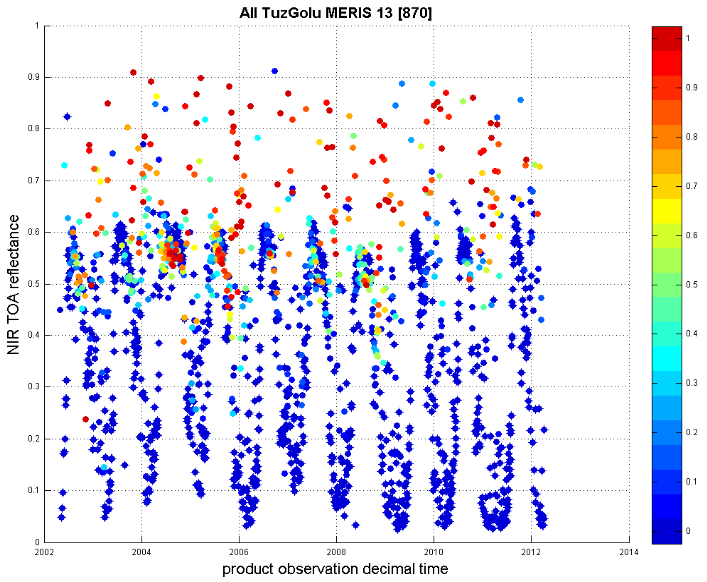

Figure 16: NIR TOA reflectance versus acquisition time. Cloud coverage level is indicated with colortable.

3.4.3.8 Libya4

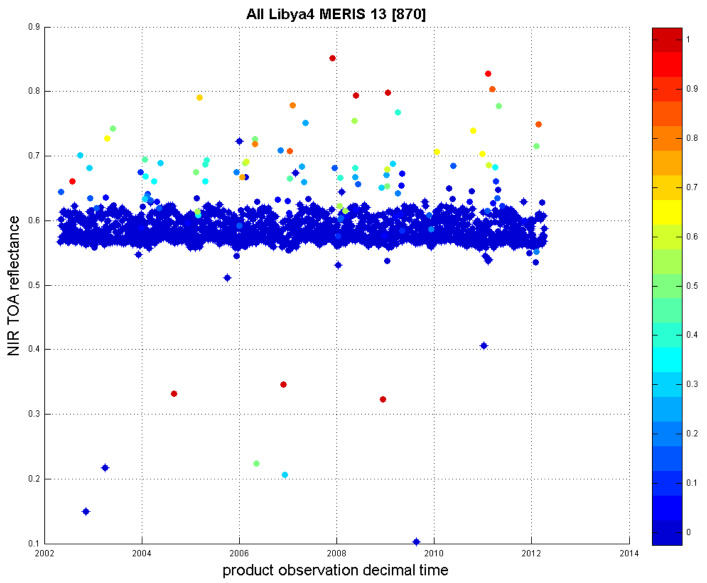

Figure 17: NIR TOA reflectance versus acquisition time. Cloud coverage level is indicated with colortable.

3.4.4 ATSR2

3.4.4.1 SIO

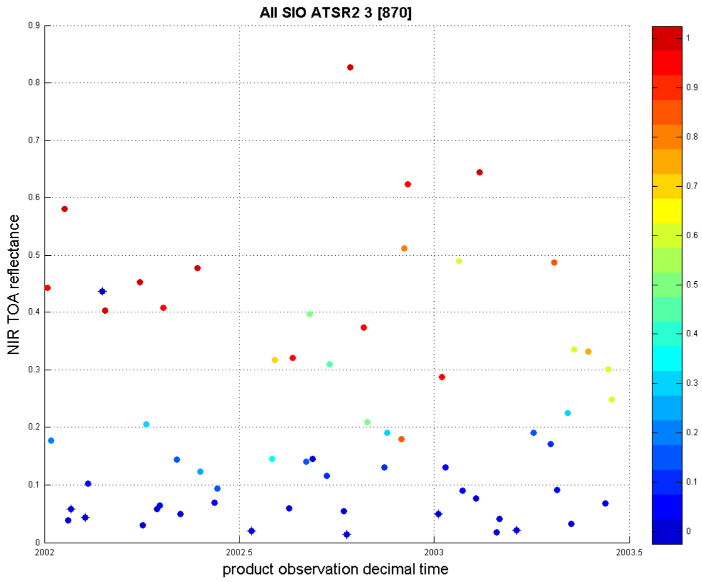

Figure 18: NIR TOA reflectance versus acquisition time. Cloud coverage level is indicated with colortable.

3.4.4.2 SPG

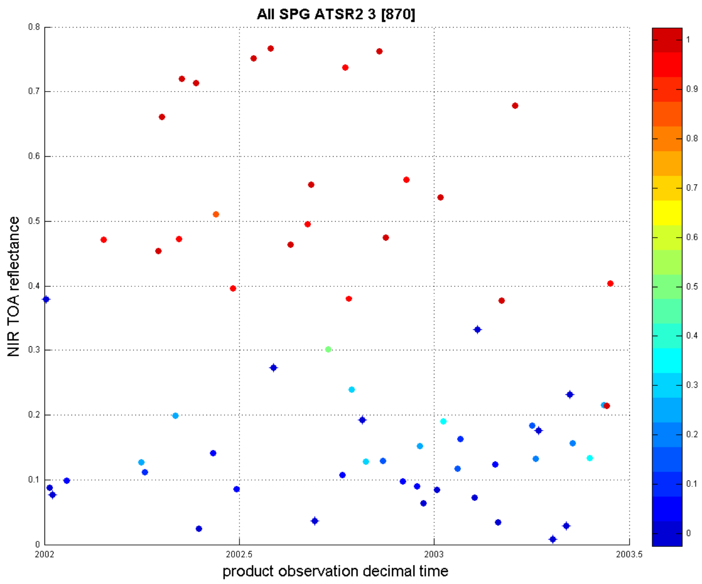

Figure 19: NIR TOA reflectance versus acquisition time. Cloud coverage level is indicated with colortable.

3.4.4.3 Boussole

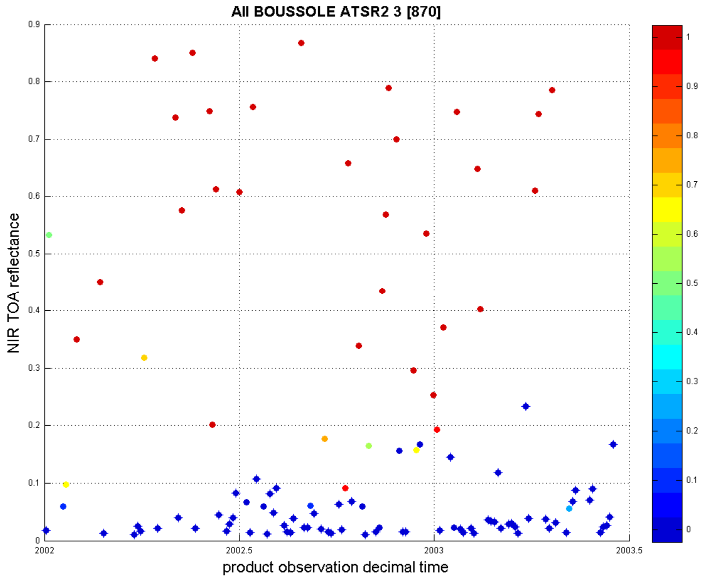

Figure 20: NIR TOA reflectance versus acquisition time. Cloud coverage level is indicated with colortable.

3.4.4.4 Amazon

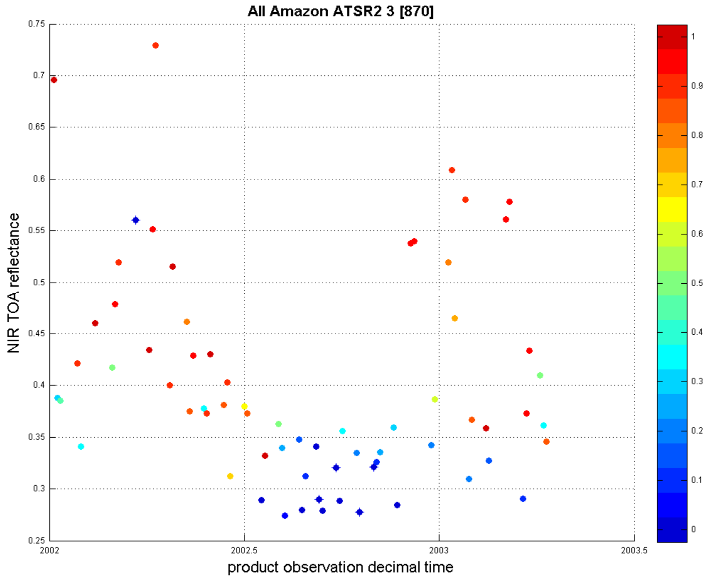

Figure 21: NIR TOA reflectance versus acquisition time. Cloud coverage level is indicated with colortable.

3.4.4.5 DomeC

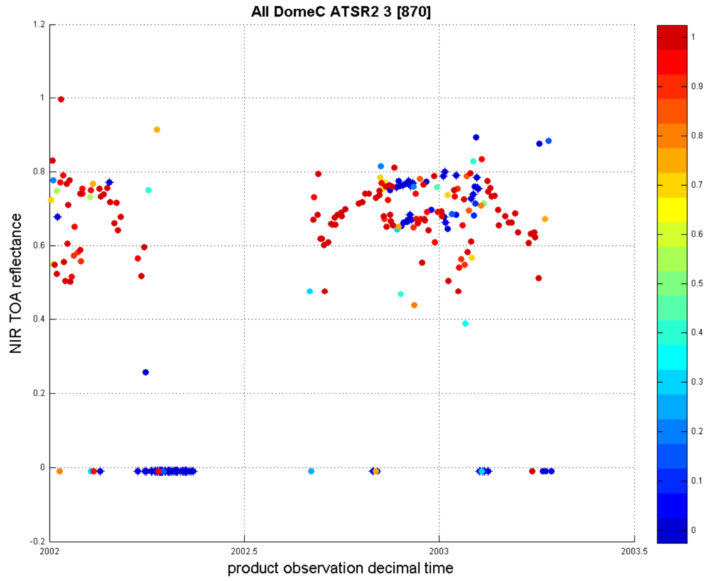

Figure 22: NIR TOA reflectance versus acquisition time. Cloud coverage level is indicated with colortable.

3.4.4.6 Uyuni

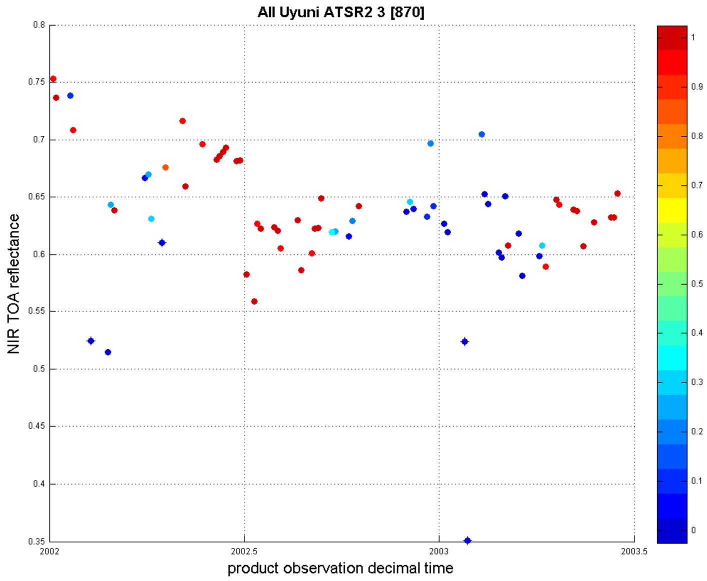

Figure 23: NIR TOA reflectance versus acquisition time. Cloud coverage level is indicated with colortable.

3.4.4.7 TuzGolu

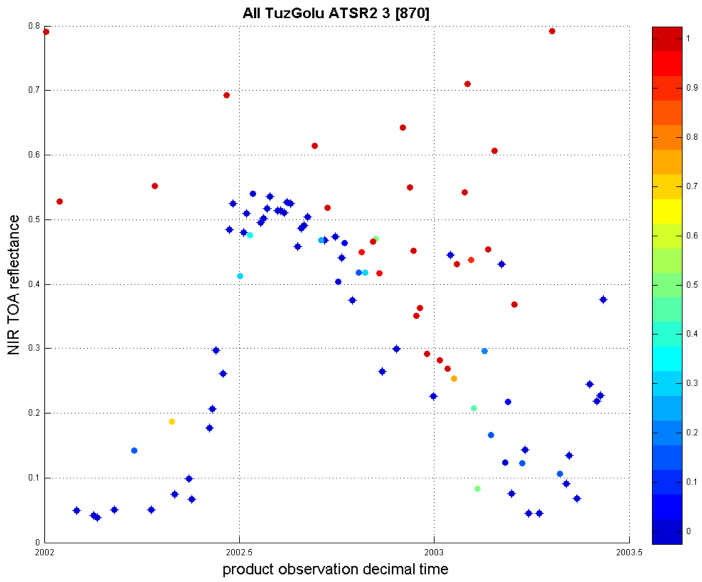

Figure 24: NIR TOA reflectance versus acquisition time. Cloud coverage level is indicated with colortable.

3.4.4.8 Libya4

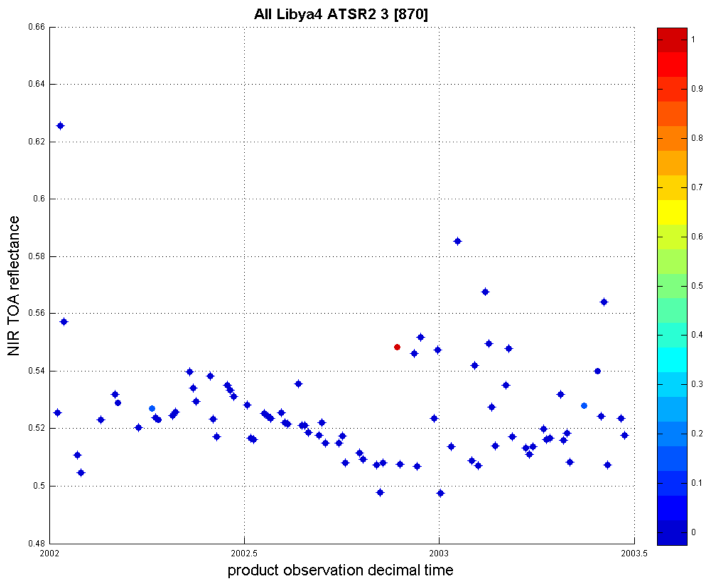

Figure 25: NIR TOA reflectance versus acquisition time. Cloud coverage level is indicated with colortable.

3.4.5 AATSR

3.4.5.1 SIO

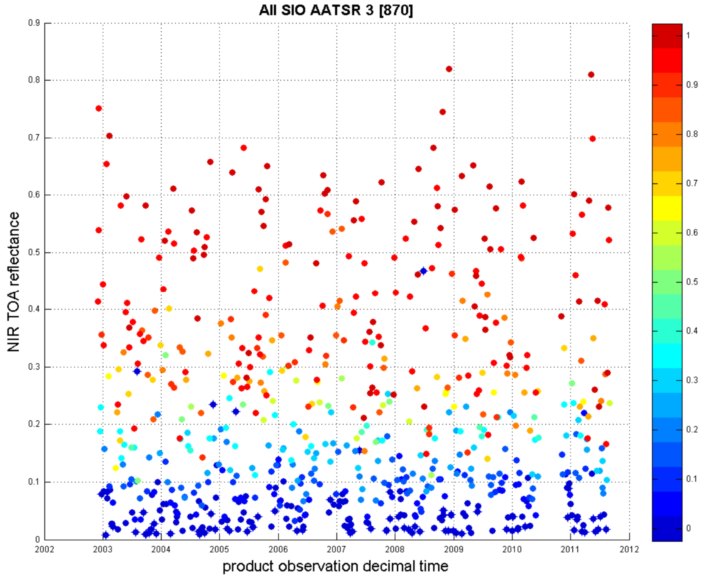

Figure 26: NIR TOA reflectance versus acquisition time. Cloud coverage level is indicated with colortable.

3.4.5.2 SPG

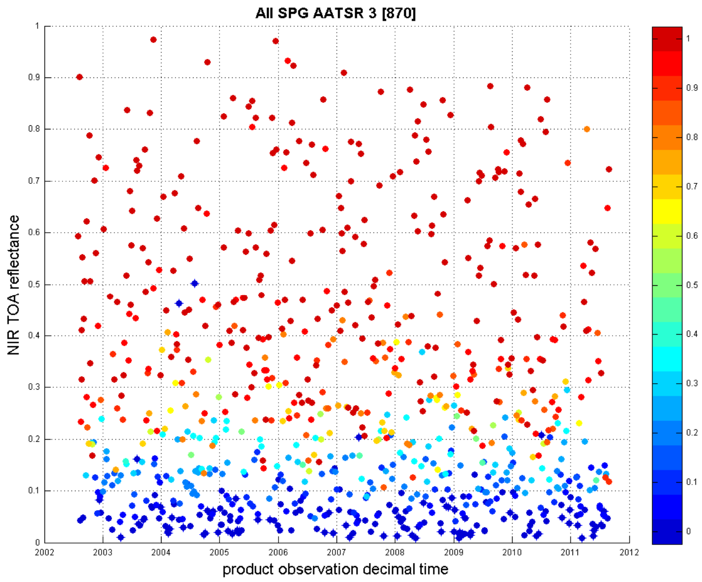

Figure 27: NIR TOA reflectance versus acquisition time. Cloud coverage level is indicated with colortable.

3.4.5.3 Boussole

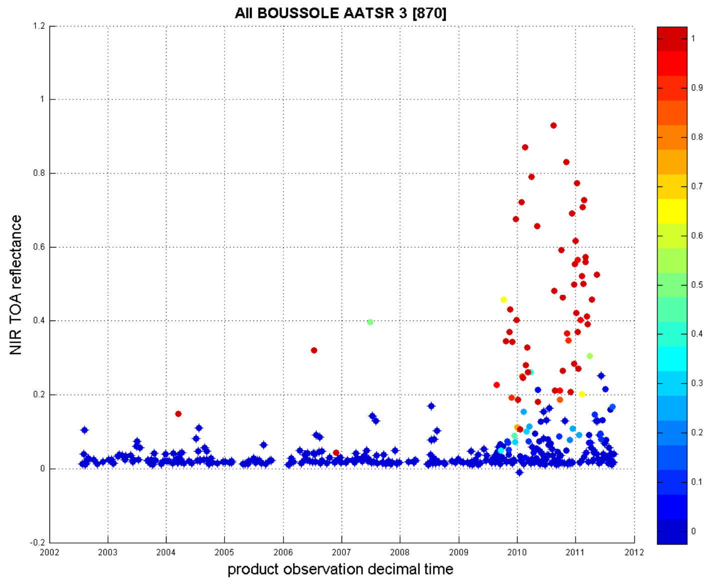

Figure 28: NIR TOA reflectance versus acquisition time. Cloud coverage level is indicated with colortable.

3.4.5.4 Amazon

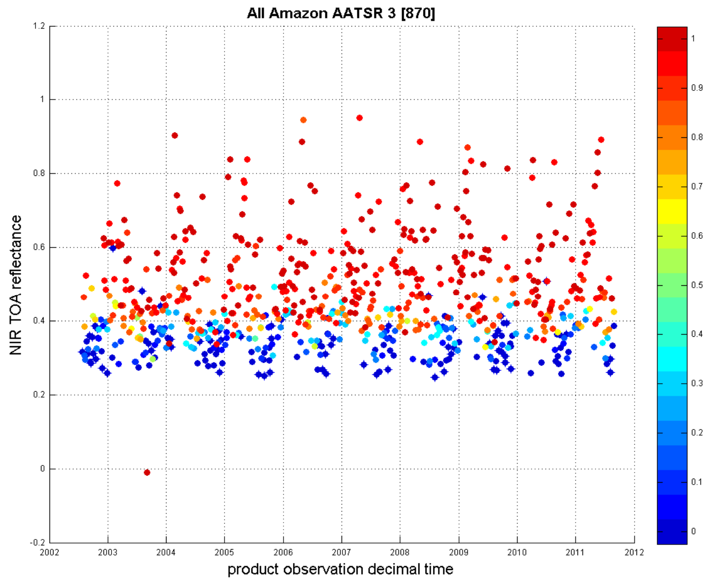

Figure 29: NIR TOA reflectance versus acquisition time. Cloud coverage level is indicated with colortable.

3.4.5.5 DomeC

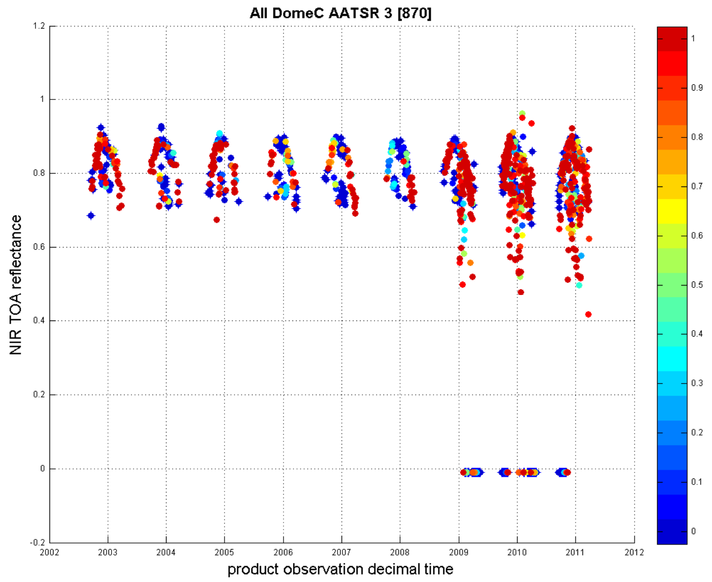

Figure 30: NIR TOA reflectance versus acquisition time. Cloud coverage level is indicated with colortable.

3.4.5.6 Uyuni

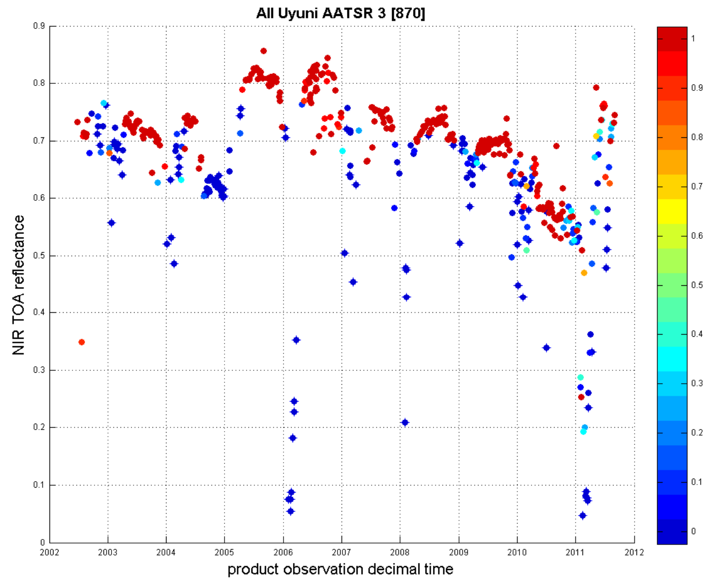

Figure 31: NIR TOA reflectance versus acquisition time. Cloud coverage level is indicated with colortable.

3.4.5.7 TuzGolu

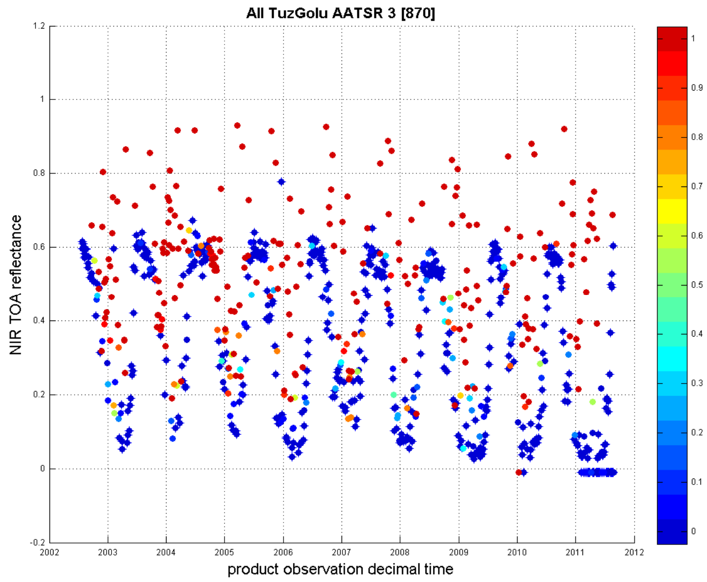

Figure 32: NIR TOA reflectance versus acquisition time. Cloud coverage level is indicated with colortable.

3.4.5.8 Libya4

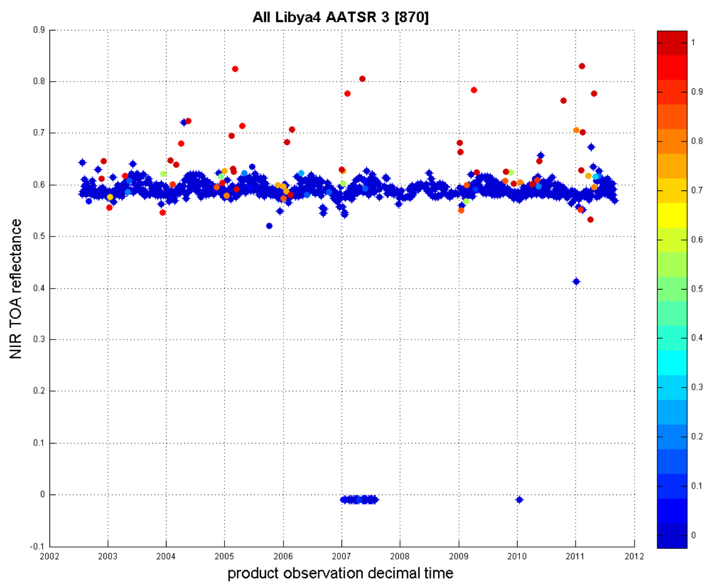

Figure 33: NIR TOA reflectance versus acquisition time. Cloud coverage level is indicated with colortable.

3.4.6 PARASOL

3.4.6.1 SIO

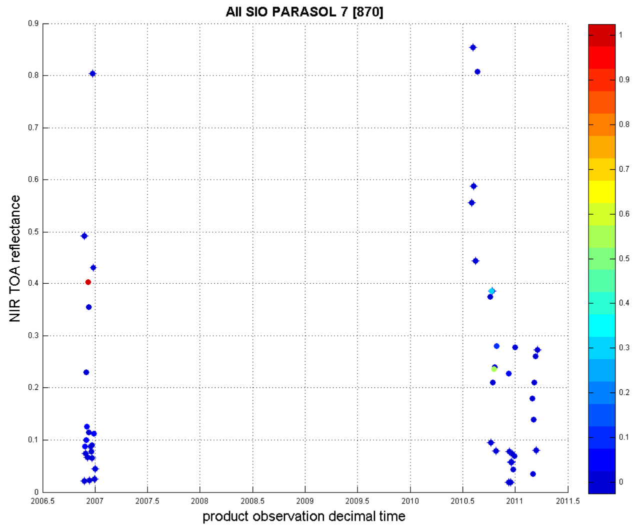

Figure 34: NIR TOA reflectance versus acquisition time. Cloud coverage level is indicated with colortable.

3.4.6.2 SPG

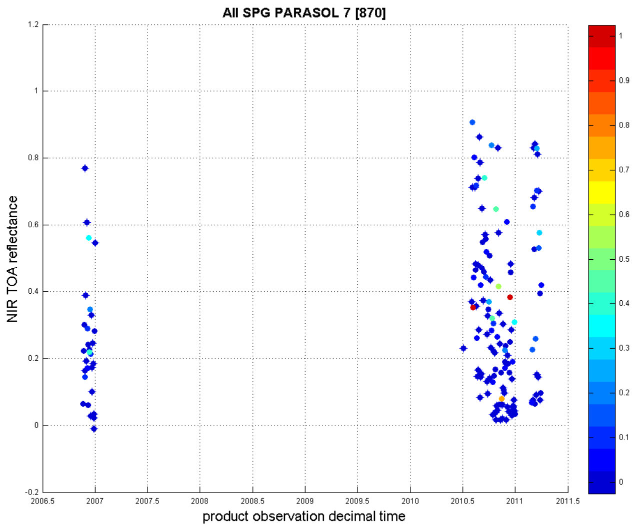

Figure 35: NIR TOA reflectance versus acquisition time. Cloud coverage level is indicated with colortable.

3.4.6.3 Boussole

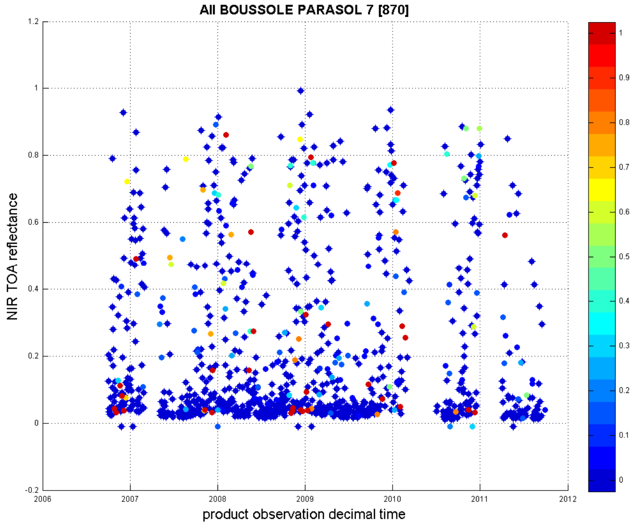

Figure 36: NIR TOA reflectance versus acquisition time. Cloud coverage level is indicated with colortable.

3.4.6.4 Amazon

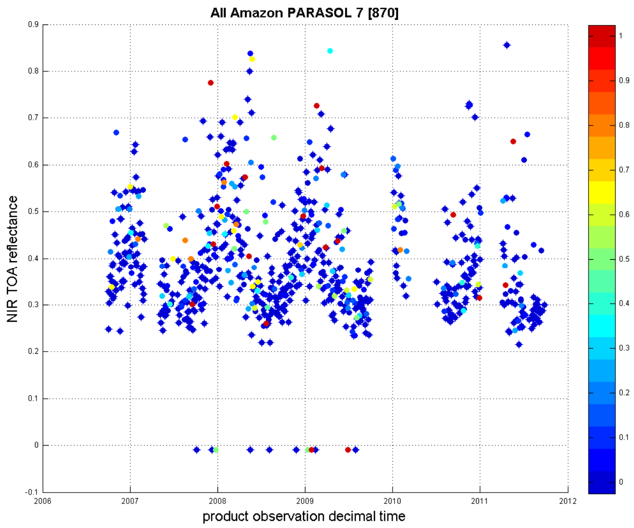

Figure 37: NIR TOA reflectance versus acquisition time. Cloud coverage level is indicated with colortable.

3.4.6.5 DomeC

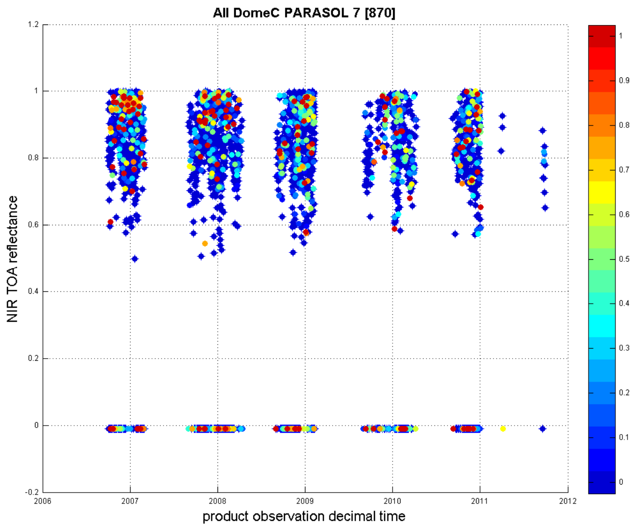

Figure 38: NIR TOA reflectance versus acquisition time. Cloud coverage level is indicated with colortable.

3.4.6.6 Uyuni

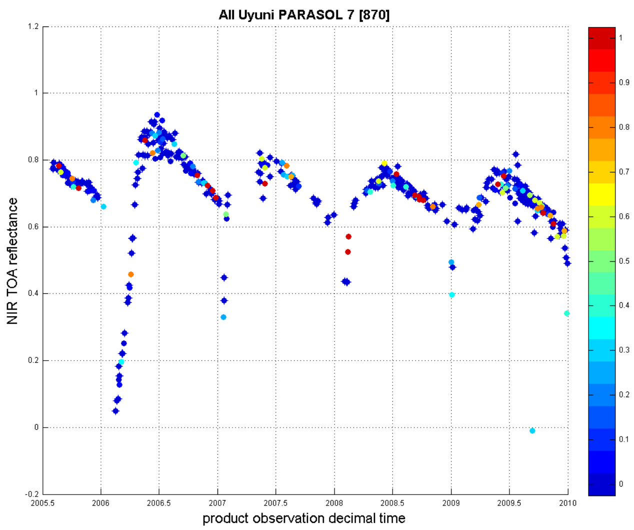

Figure 39: NIR TOA reflectance versus acquisition time. Cloud coverage level is indicated with colortable.

3.4.6.7 TuzGolu

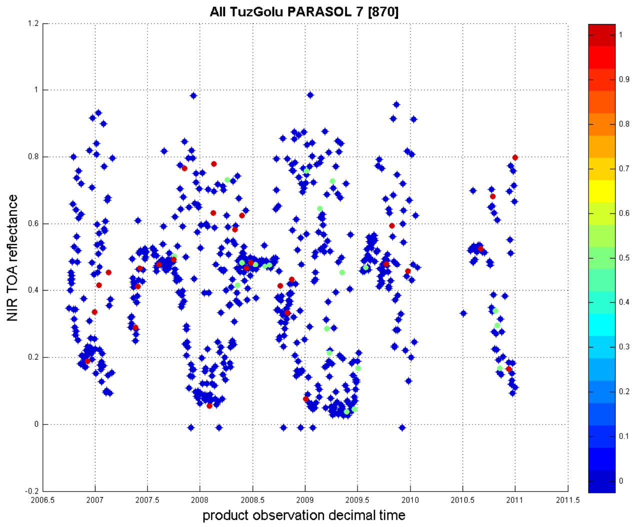

Figure 40: NIR TOA reflectance versus acquisition time. Cloud coverage level is indicated with colortable.

3.4.6.8 Libya4

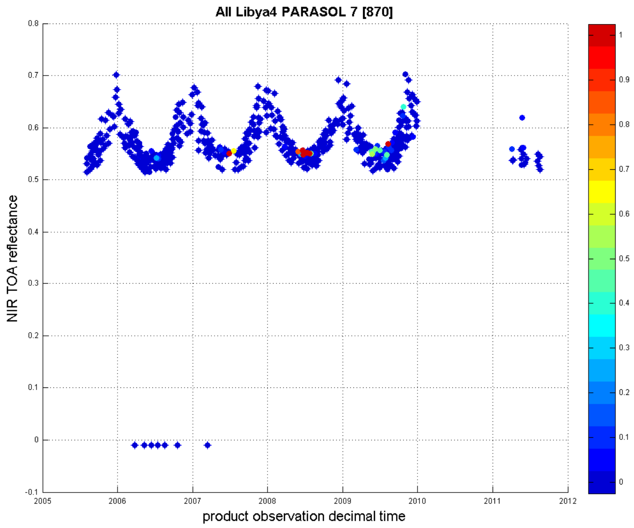

Figure 41: NIR TOA reflectance versus acquisition time. Cloud coverage level is indicated with colortable.

3.4.7 VEGETATION

3.4.7.1 SIO

N/A

3.4.7.2 SPG

N/A

3.4.7.3 Boussole

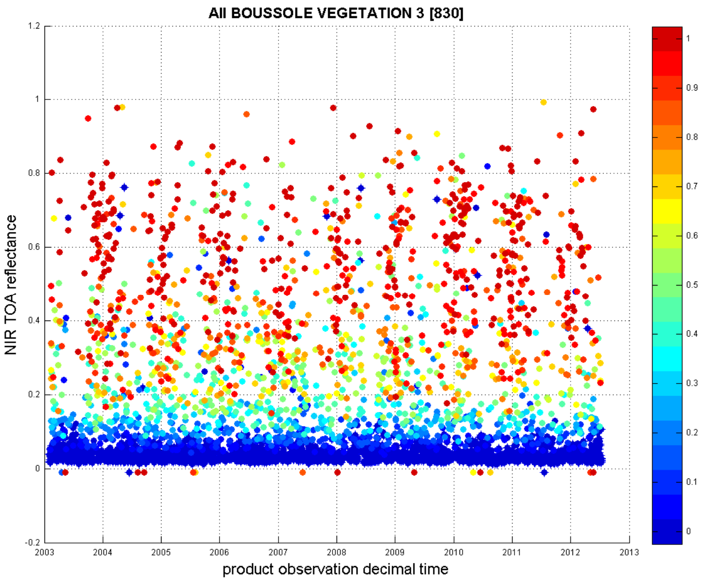

Figure 42: NIR TOA reflectance versus acquisition time. Cloud coverage level is indicated with colortable.

3.4.7.4 Amazon

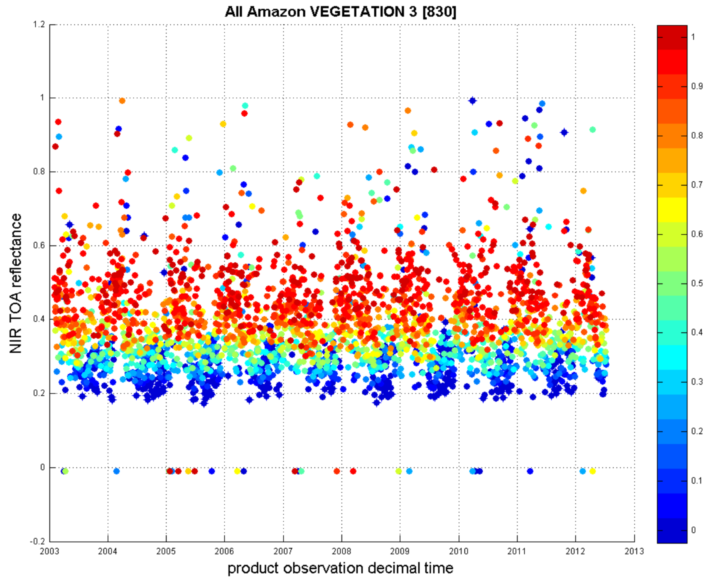

Figure 43: NIR TOA reflectance versus acquisition time. Cloud coverage level is indicated with colortable.

3.4.7.5 DomeC

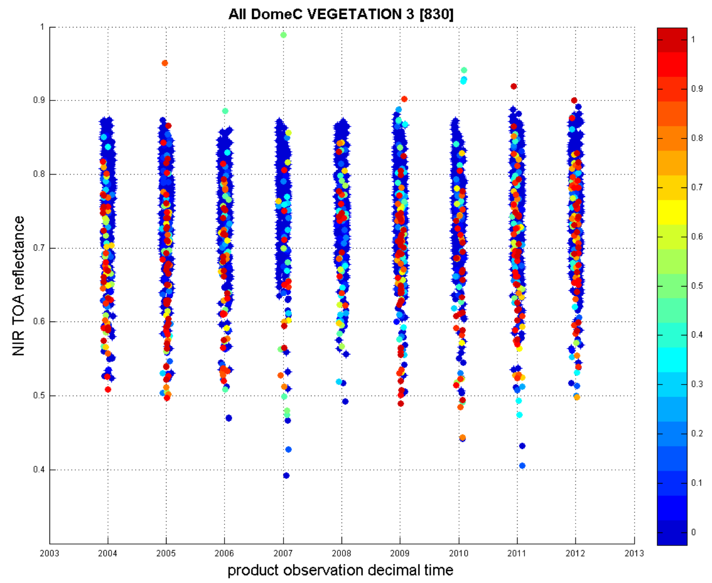

Figure 44: NIR TOA reflectance versus acquisition time. Cloud coverage level is indicated with colortable.

3.4.7.6 Uyuni

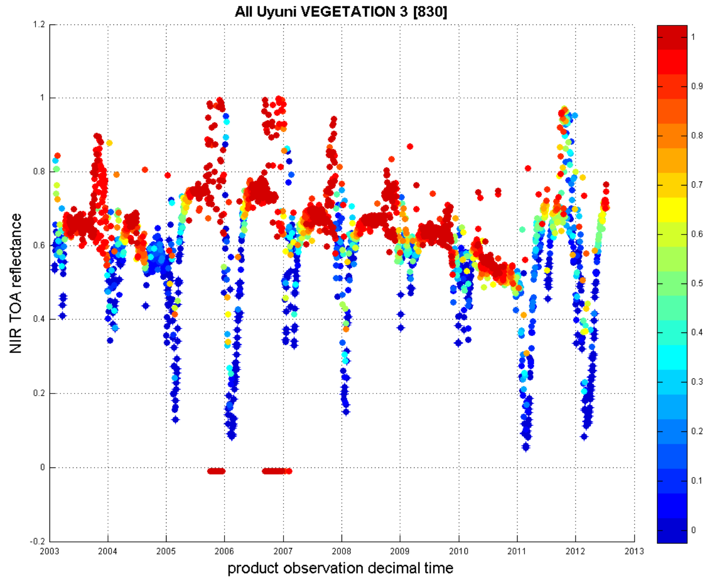

Figure 45: NIR TOA reflectance versus acquisition time. Cloud coverage level is indicated with colortable.

3.4.7.7 TuzGolu

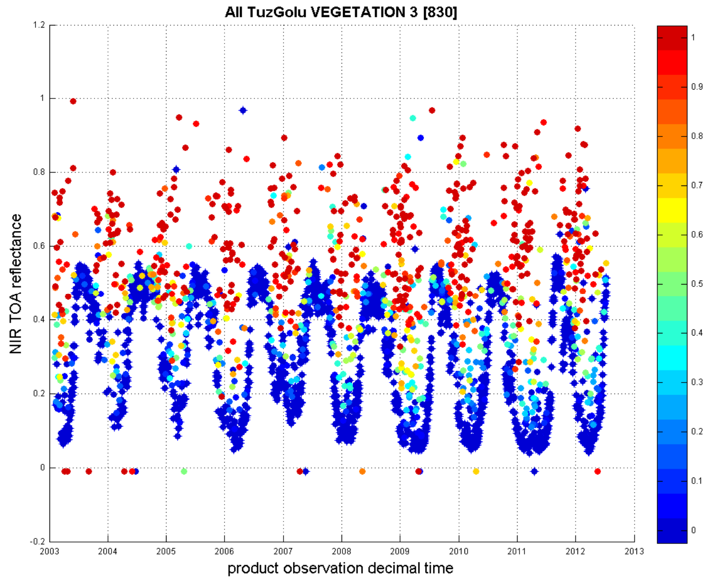

Figure 46: NIR TOA reflectance versus acquisition time. Cloud coverage level is indicated with colortable.

3.4.7.8 Libya4

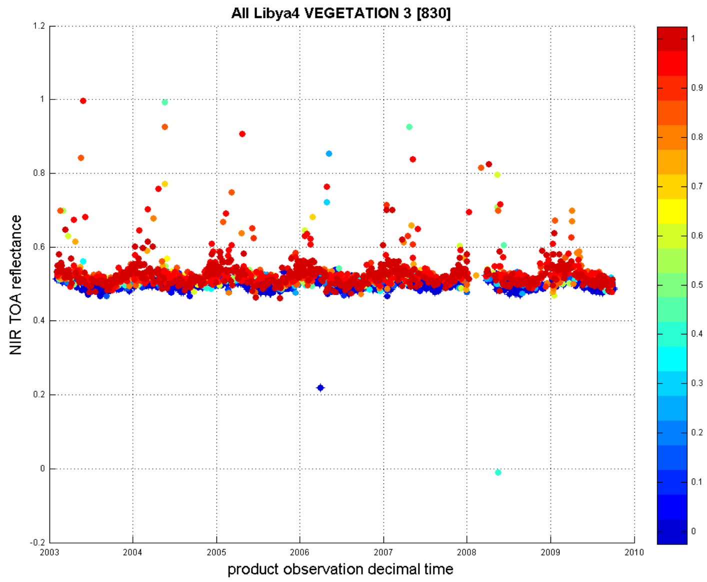

Figure 47: NIR TOA reflectance versus acquisition time. Cloud coverage level is indicated with colortable.

3.5 Synthesis of the analysis

3.5.1 Overview of the results

The following table provides an overview of the performance of the cloud detection performed using DIMITRI V2.

- O stands for overestimation: It is highlighted when a blue color (low level of cloud coverage) is found with high reflectance.
- U stands for underestimation. It is highlighted when a red color (high level of cloud coverage) is found with low reflectance.
- ☺ means that the cloud coverage level is coherent with the level of reflectance.

The results are macrospopic since they are based on mean values of TOA reflectances and do not illustrate the spatial representativeness of the cloud mask. However, it is a good indicator of the quality.

Table 6: Performance of the cloud screening

	MODIS	MERIS	PARASOL	AATSR	ATSR-2	VEGETATION
SIO☹ ☺	U A few O ☹	A few U ☺	O	☺	☺	N/A
SPG	U A few O ☹	A few U ☺	O	☺	☺	N/A
Boussole	U A few O	A few U ☺	O	A few U ☺	☺	A few U ☺
Amazon	U A few O	A few U ☺	☺	O	O	A few U ☺
DomeC	O	No clouds ? TBC	TBC	O	O TBC	TBC
Uyuni	O	O	A few O ☺	O	O	O
TuzGulu	A few U O	A few U ☺	U	☺	☺	A few U ☺
Libya4	A few U A few O	☺	☺	☺	A few O ☺	O

3.5.2 Roadmap for improvement of the cloud detection

3.5.2.1 Over invariant sites (SIO, SPG, BOUSSOLE, Libya4)

3.5.2.1.1 Over ocean sites

The reflectance of the site could strongly change if the data are acquired in conditions of specular reflection of the sun on the ocean surface.

The separation of data acquired inside and outside sunglint is the first step to implement before testing again the algorithms implemented.

The ocean sites have been chosen due to their low variability of surface reflectance. Their reflectance is predictable, knowing the atmospheric component variability. Based on this, the same thresholds could be used to detect the clouds for all sensors.

For Boussole, the same approach is still valid, except that the level of TOA reflectance is higher than over SIO and SPG.

The following figures represent the variability of the TOA reflectance of the NIR channels for the case where the cloud coverage is 0.

Cloud underdetections are clearly visible, in particular for MODIS and PARASOL data.

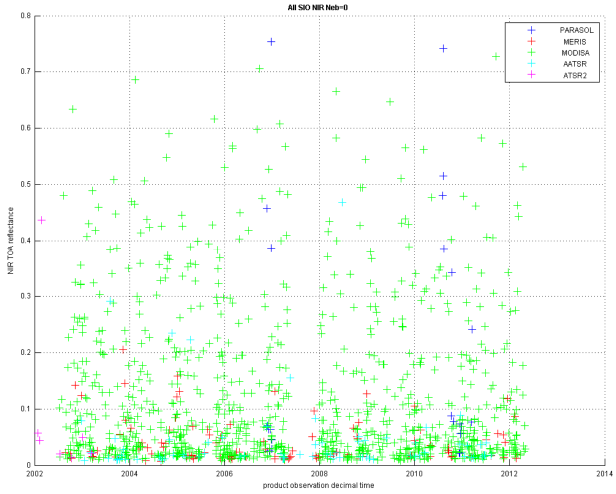

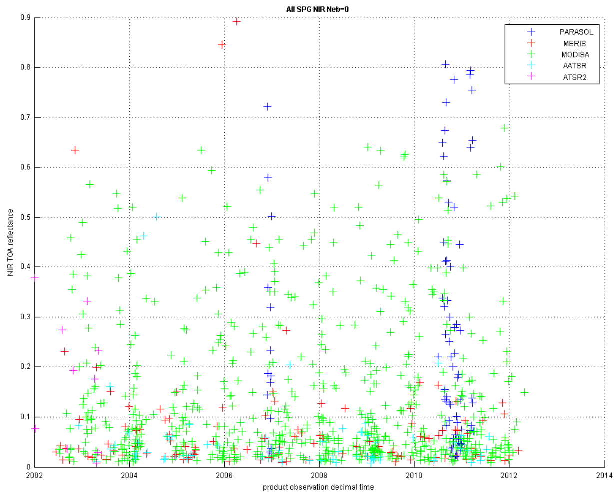

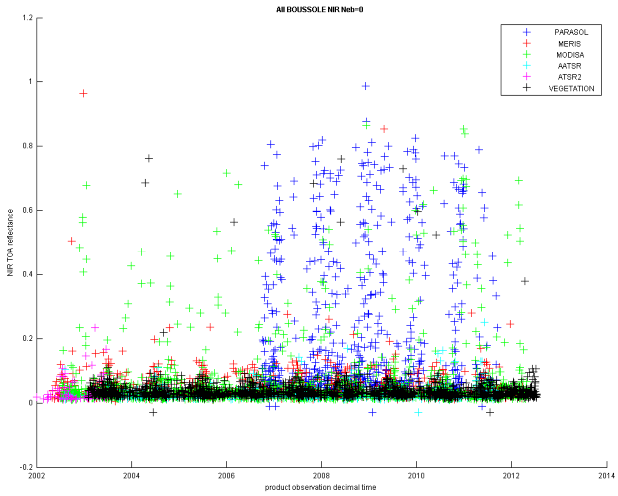

Figure 48: NIR TOA reflectance variability versus acquisition time for acquisition where cloud coverage is zero. SIO, SPG and Boussole site.

3.5.2.1.2 Over desert (Libya4)

The cloud detection over the desert site Libya 4 is good for all sensors except VEGETATION for which thresholds seems to be adapted. VEGETATION NIR central band is located at 830 nm whereas it is located around 870 nm for the other sensors.

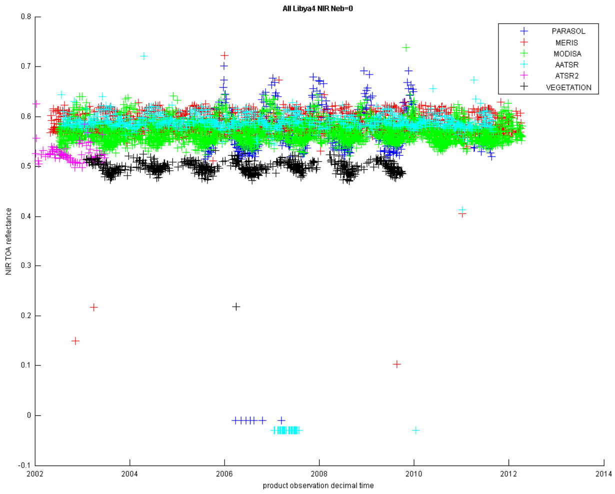

Figure 49: NIR TOA reflectance variability versus acquisition time for acquisition where cloud coverage is zero. Libya 4 site.

3.5.2.2 Over non invariant sites

3.5.2.2.1 Over Salty sites: Uyuni, TuzGulu

The analysis of the temporal profiles of NIR TOA reflectances highlights that the evolution of the reflectance is not identical from one year to another one year.

Where the cloud detection thresholds seem well adapted to TuzGulu, it seems less adapted to Uyuni, except for PARASOL data.

The sites are not invariant, even the Tuzgulu highlights a cycle which makes fall the reflectance due to presence of water at some seasons.

Typically, the thresholds used in the algorithm should be adapted specifically to each site to improve the performance of the detection.

In particular, PARASOL and MERIS cloud detection need to be improved over TuzGulu to correct the cloud underdetection.

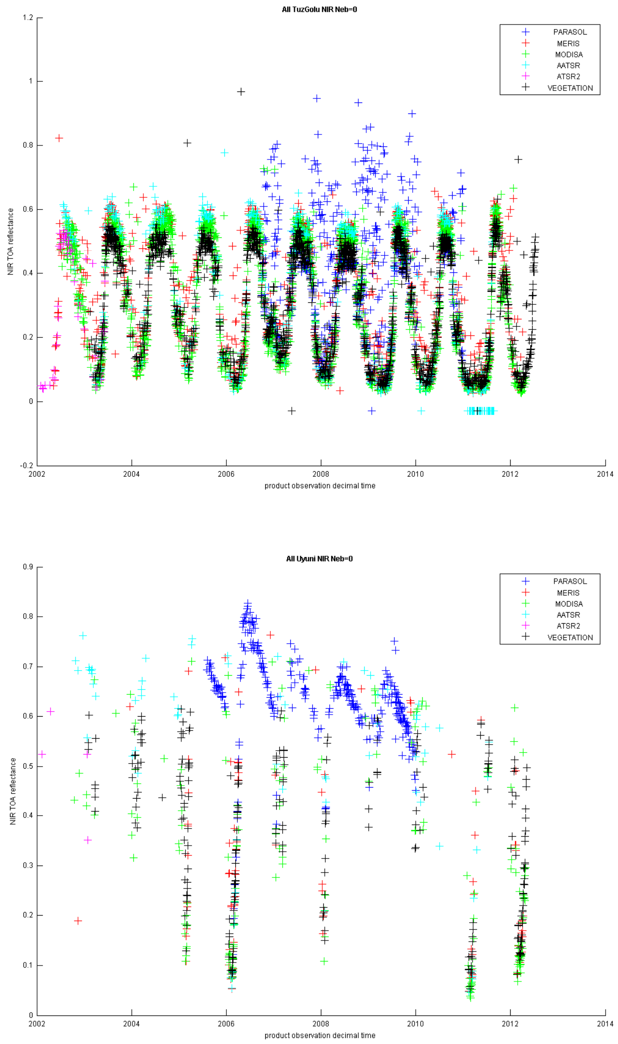

Figure 50: NIR TOA reflectance variability versus acquisition time for acquisition where cloud coverage is zero. TuzGulu, Uyuni sites.

3.5.2.2.2 Over forest site (Amazon)

The cloud detection is good, except a few underdetection for PARASOL.

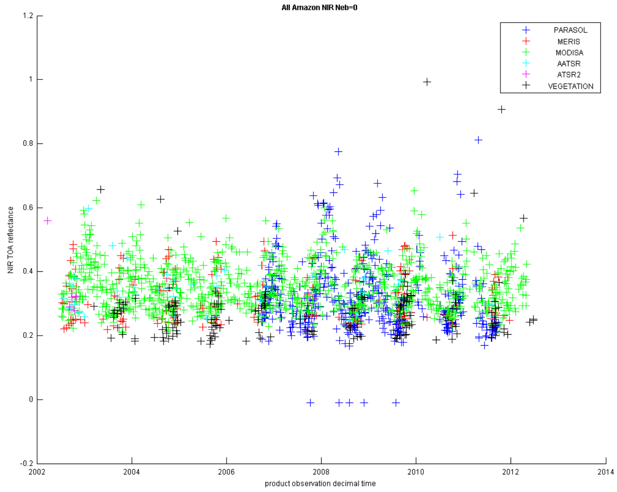

Figure 51: NIR TOA reflectance variability versus acquisition time for acquisition where cloud coverage is zero. Amazon sites.

3.5.2.2.3 Over Snow site (DomeC)

The results are difficult to interpret because there are cases of full over or under cloud detection, for all sensors except AATSR and ATSR2 where cloudy pixels have been detected.

The evaluation needs to be performed on images.

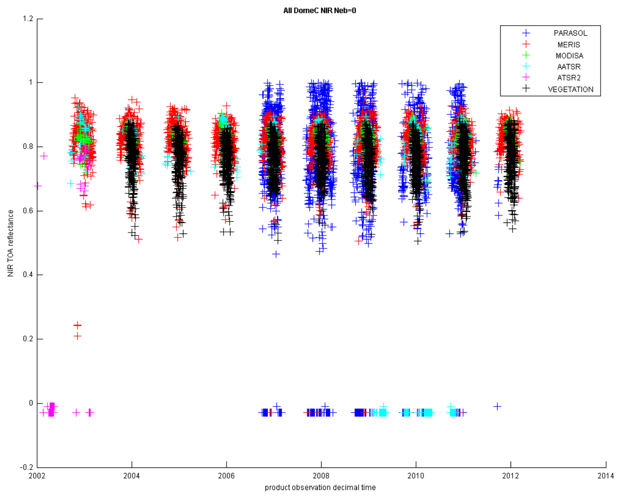

Figure 52: NIR TOA reflectance variability versus acquisition time for acquisition where cloud coverage is zero. Dome C sites.

4 Algorithm improvement description

4.1 Approach

The analysis of reference dataset previously described highlighted the need for some sensors over specific sites to improve the cloud detection. For a group of sites, such as they are defined in DIMITRI, the algorithms are analyzed in order to provide with a figure where the TOA reflectances times series are coherent with time, and where over or under detection are eliminated.

The approach is different than the one used in DIMITRI v2. The algorithms are rather adapted to the site characteristics, and only three flags are defined:

- INVALID;
- CLOUD;
- CLEAR.

The methods implemented are clear-sky conservative, which suits well for calibration activities.

- A pixel is defined as cloud free if all spectral measures fall on the "clear-sky" sides of the various thresholds.
- A pixel is defined as cloud contaminated if it fails any single test.

The implementation is defined by the following steps:

- Step 1: The mask is initialized.
- Step 2: At each test, a Cloud mask is filled
- Step 3: The total coverage is computed as the product of each cloud mask
- Step 4: The spatial coherence test is applied to the cloud mask.
- Step 5: The final mask is dilated
- Step 6: The cloud coverage is estimated by counting the number of cloudy pixels to the total number of pixels contained in the site.

INVALID data is kept in the processing.

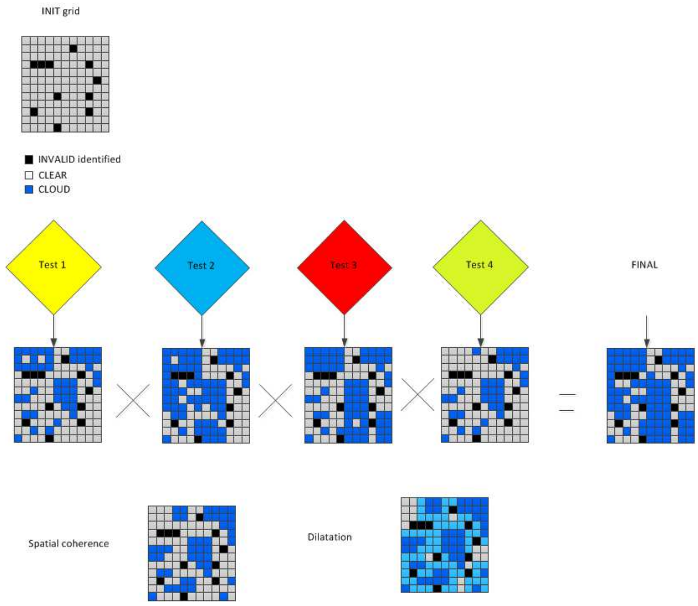

Figure 53: Chaining of the steps

4.1.1 Over ocean

Improvements could be made to the cloud mask in sun-glint regions and in daytime oceans by applying a tree decision to separate acquisitions inside and outside glitter area. This concerns SIO, SPG and BOUSSOLE sites.

Sun glint occurs in imagery when the water surface orientation is such that the sun is directly reflected towards the sensor; and hence is a function of sea surface state, sun position and viewing angle. Different methods have been documented. In MODIS case (Ackerman et al., 1998), the sunglint is defined in the cloud mask algorithm using a purely geometrical approach.

Sun glint processing path is taken when the reflected sun angle, θ_r, lies between 0° and approximately 36°,where

$$\cos(\theta_r) = \cos(\theta_s)\cos(\theta_v) + \sin(\theta_s)\sin(\theta_v)\cos(d\phi)$$

Where θ_s is the solar zenith angle and ϕ_s the azimuth angle; θ_v is the viewing zenith angle and ϕ_v the azimuth angle. $d\Phi = \phi_s - \phi_v$

0 defines the specular point.

This figure illustrates the variability of clear sky observations in the NIR versus the sun-glint angle.

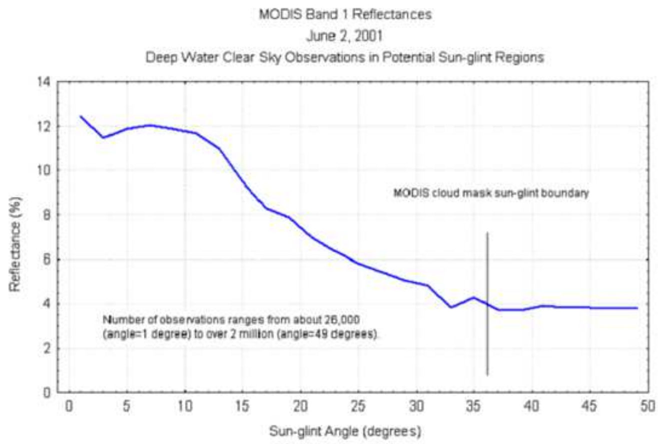

Figure 54: MODIS channel 2 reflectance as a function of reflectance angle, on June 2, 2001 over ocean regions.

In POLDER, as a second case, the off-sunglint 865-nm maximal radiance threshold is 0.005 in normalized radiance units

MODIS approach is selected to separate the observations and applying different thresholds depending on the angular region.

4.1.1.1 MODIS cloud detection

The algorithm has been changed and is based on MODIS ATBD. Additional thresholds have been implemented. It used the NIR and VIS reflectance, cirrus channel at 1.38 µm, and the temperature at 11 µm.

The processing is the same inside sunglint areas or outside sunglint areas, only specific thresholds have been set to detect cloud over sunglint.

Tests and Thresholds are reported in the table below.

Table 7: Overview of tests and Thresholds

Tests	Detect as cloud if	Threshold s	Thresholds for Sunglint path
Select VALID pixels in VIS and NIR			
Test on NIR reflectance	$\rho > T1$	0.045	T1 estimated as a function of θ_r (see Figure 54)
Test on NIR/VIS ratio	$\rho NIR / \rho VIS > T2$	0.85	1.025
Test on Cirrus	$\rho > T3$	T3=0.03	T3=0.03
Test on BT 12 µm	desactivated	N/A	N/A
Spatial coherence	For a window of 3x3 pixels $\sigma >$ T5_sdt OR abs(ρ-ρ mean) > T5_avg	T5_sdt = 0.01 T5_avg=0.01	T5_sdt = 0.015 T5_avg=0.015
Dilatation of cloud mask		1 pixel	1 pixel

Two examples of the cloud detection steps are shown hereafter.

4.1.1.1.1 Example 1: Cloud detection over SIO

The acquisition date is 09/01/2009. We have :

One image of Valid pixels

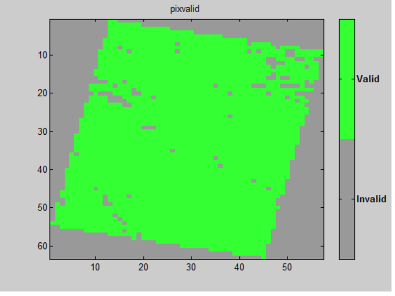

One image of NIR TOA reflectances, its histogram, its mask.

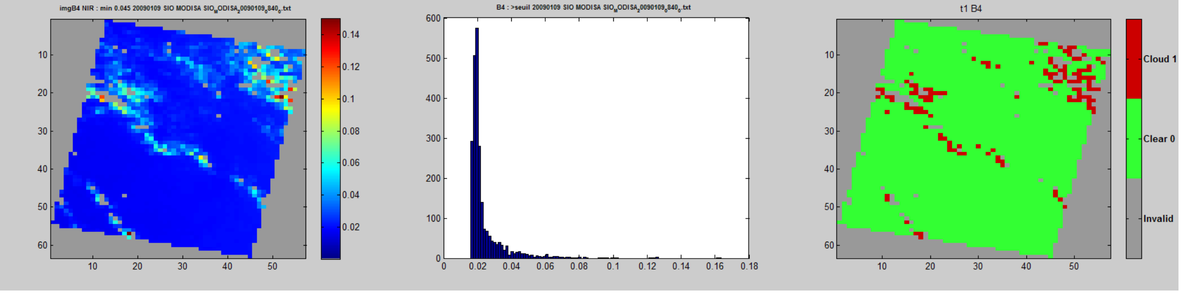

One image of NIR/VIS TOA reflectances, its histogram, its mask.

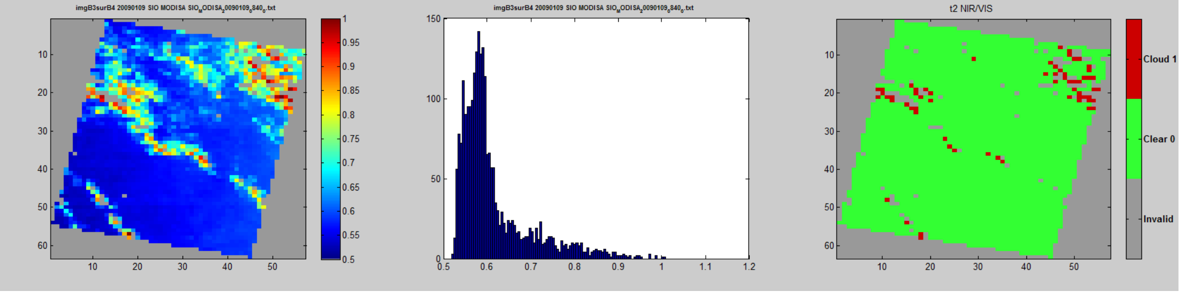

One image of BT temperature, its histogram, its mask.

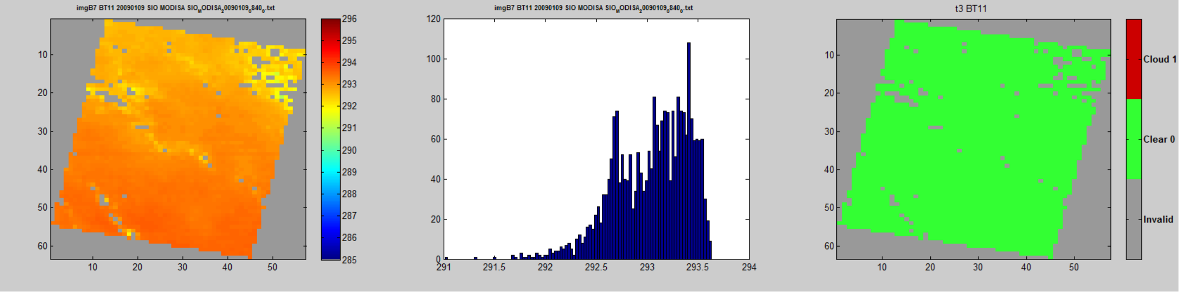

One image of Cirrus reflectance, its histogram, its mask.

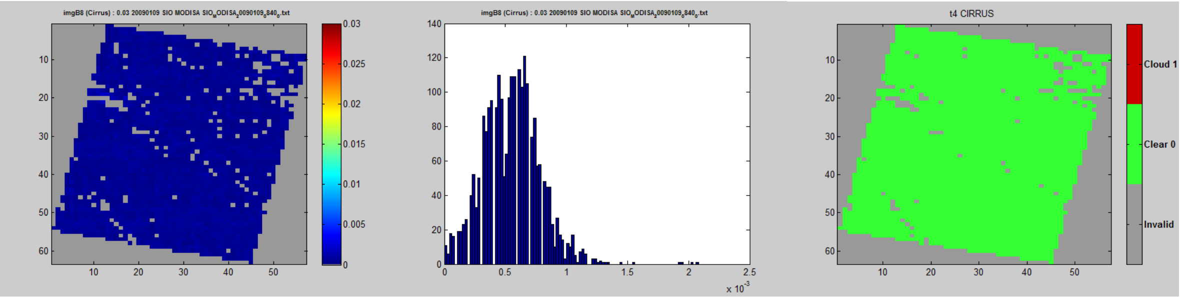

One image of spatial coherence

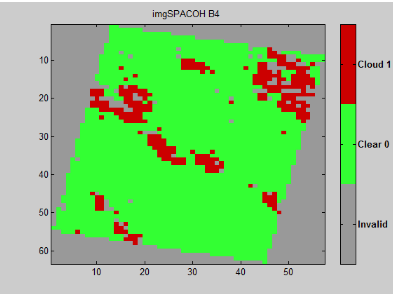

One image of the dilated mask (applied on the product of all masks)

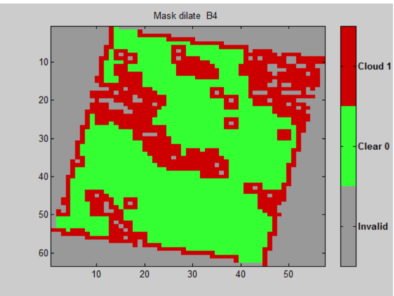

One image of final mask and its application on the NIR TOA reflectance

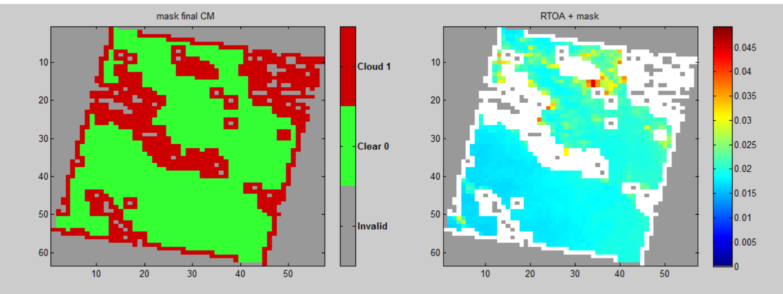

4.1.1.1.2 Example 2 : Cloud detection over SUNGLINT

These images illustrate the cloud masks to apply on the acquisition to select clear pixels.

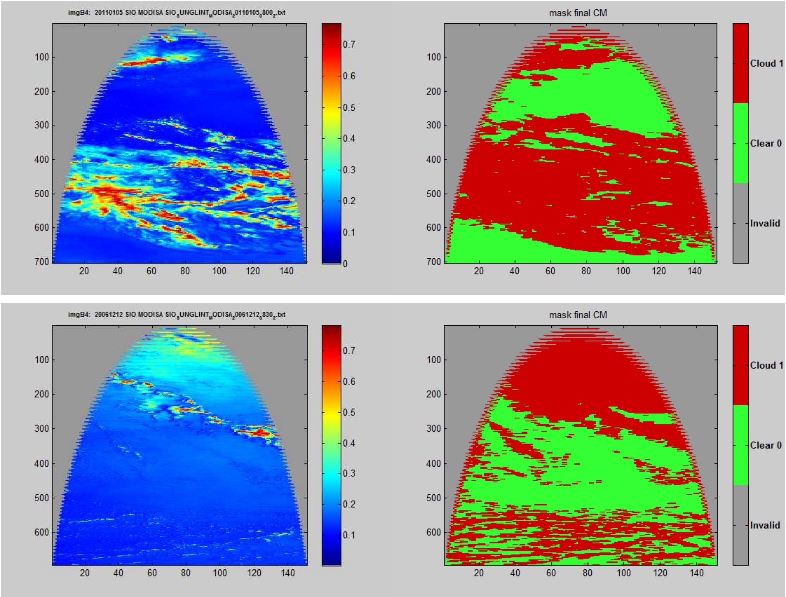

Figure 55: Cloud masks over sunglint

4.1.1.1.3 Global verification

The verification is performed by plotting the reflectances of all the channels used in the cloud detection algorithm versus the different thresholds. The pixels plotted rom a same acquisition have the same color.

These graphs allow to represent the variability of the reflectances inside the same scene.

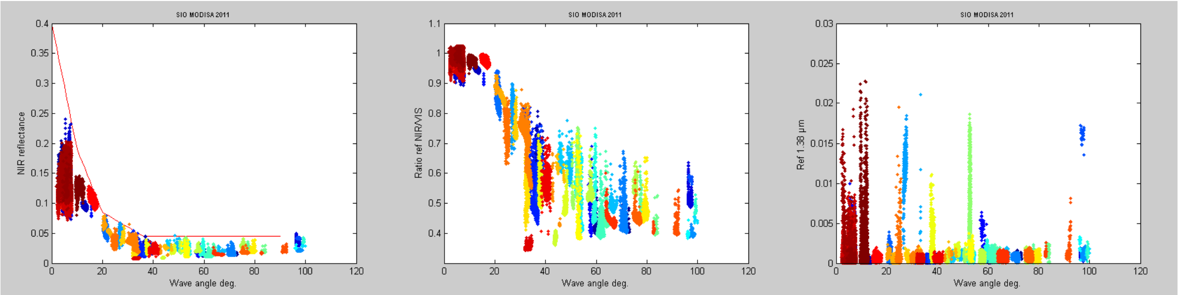

Figure 56: NIR reflectances (left), NIR/VIS reflectance ratio (middle), cirrus reflectance (right) versus wave angle.

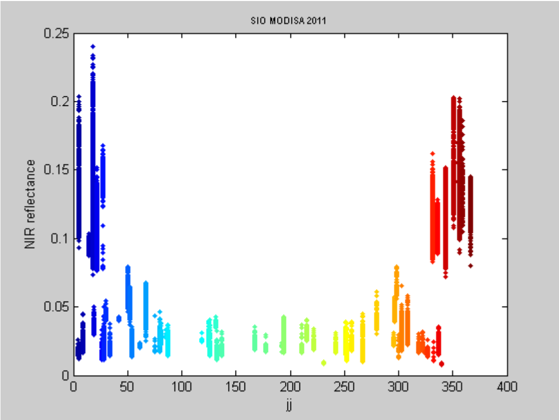

Figure 57: NIR reflectances versus Julian day.

4.1.1.2 MERIS cloud detection

The algorithm has been changed and is based on MODIS ATBD. Additional thresholds have been implemented. It used the NIR and VIS reflectance, cirrus channel at 1.38 µm, and the temperature at 11 µm.

The processing is the same inside sunglint areas or outside sunglint areas, only specific thresholds have been set to detect cloud over sunglint.

Tests and Thresholds are reported in the table below.

Table 8: Overview of tests and Thresholds

Tests	Detect as cloud if	Threshold s	Thresholds for Sunglint path
Select VALID pixels in VIS and NIR			
Test on NIR reflectance	$\rho > T1$	0.045	T1 estimated as a function of θ_r (see Figure 54)
Test on NIR/VIS ratio	$\rho NIR / \rho VIS > T2$	0.85	1.025
Spatial coherence	For a window of 3x3 pixels σ > T5_sdt OR abs(ρ-ρ mean) > T5_avg	T5_sdt = 0.01 T5_avg=0.01	T5_sdt = 0.015 T5_avg=0.015
Dilatation of cloud mask		1 pixel	1 pixel

The processing based on Bright pixels using LUTS is removed from the processing, but has been assessed. Results will be shown hereafter.

Two examples of the cloud detection steps are shown hereafter.

4.1.1.2.1 Example 1

One image of Valid pixels

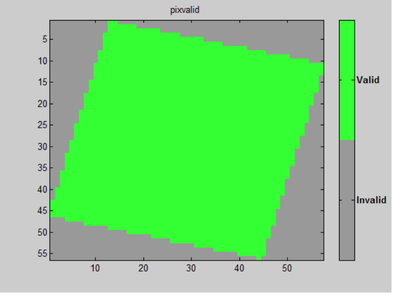

One image of cloud mask estimated using bright pixels algorithm

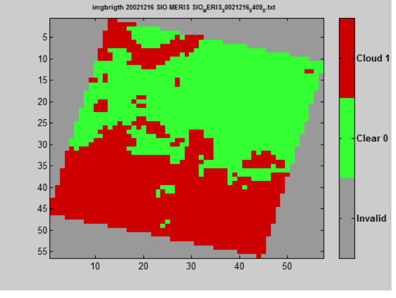

One image of NIR TOA reflectances, its histogram, its mask.

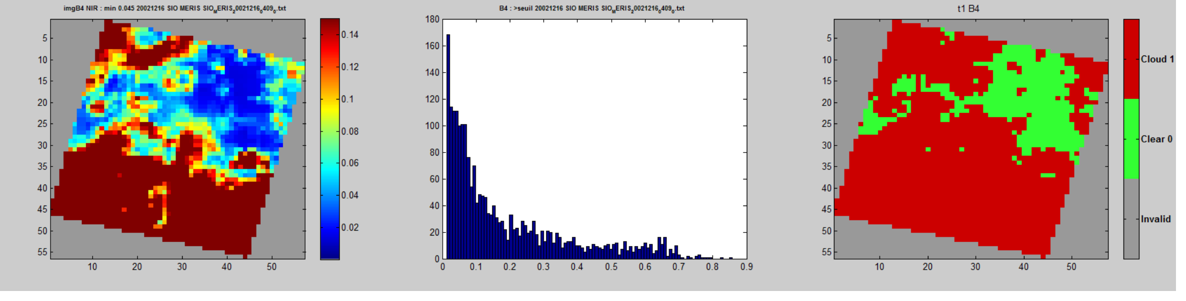

One image of NIR/VIS TOA reflectances, its histogram, its mask.

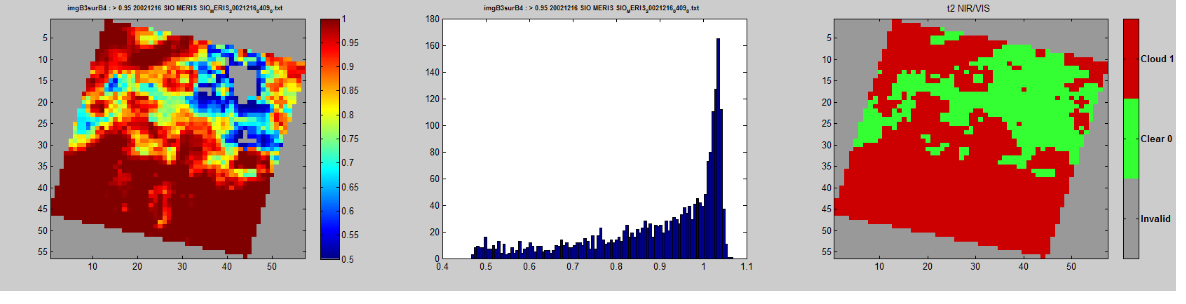

One image of spatial coherence

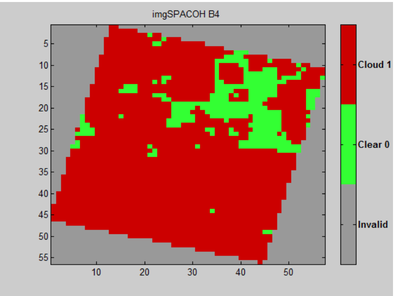

One image of the dilated mask (applied on the product of all masks)

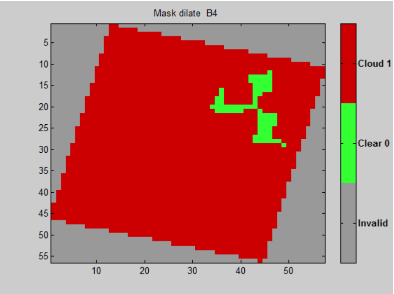

One image of final mask and its application on the NIR TOA reflectance

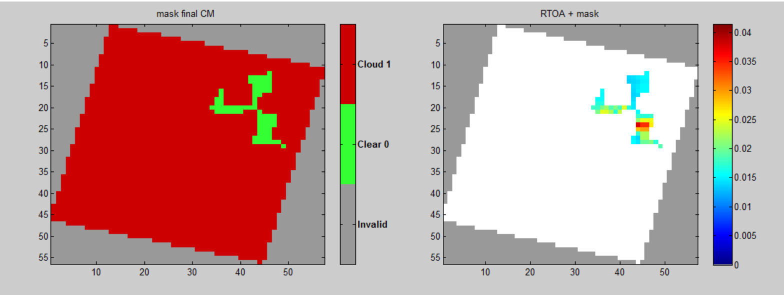

4.1.1.2.2 Example 2 over SUNGLINT

One image of Valid pixels

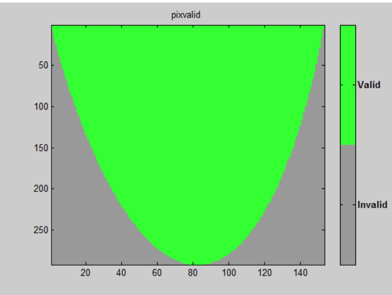

One image of cloud mask estimated using bright pixels algorithm

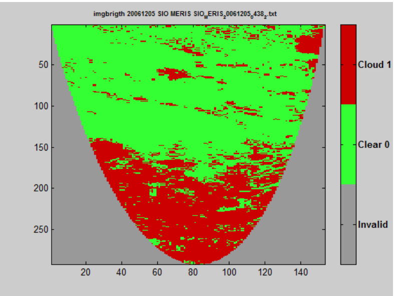

One image of NIR TOA reflectances, its histogram, its mask.

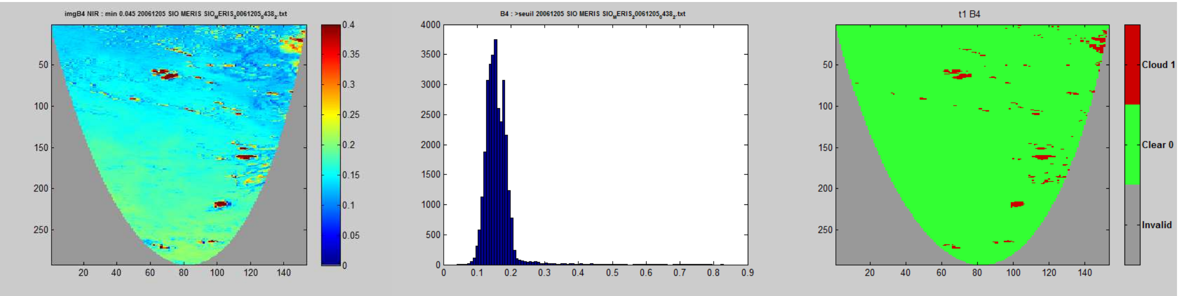

One image of NIR/VIS TOA reflectances, its histogram, its mask.

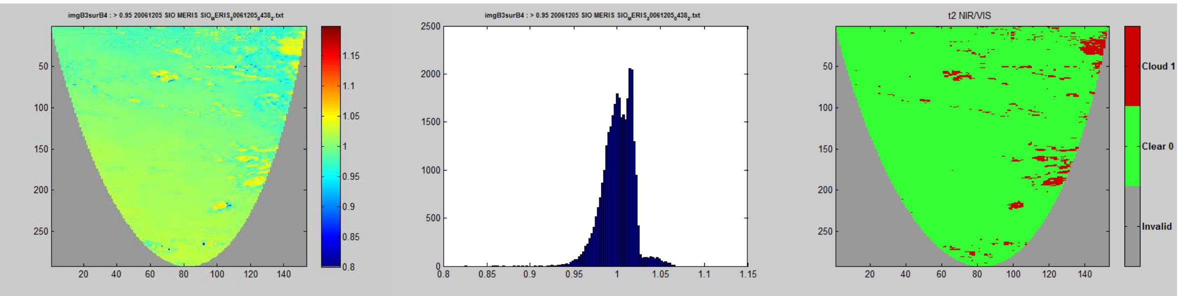

One image of spatial coherence

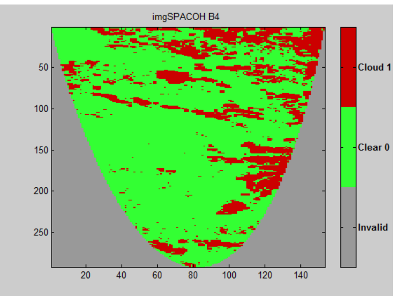

One image of the dilated mask (applied on the product of all masks)

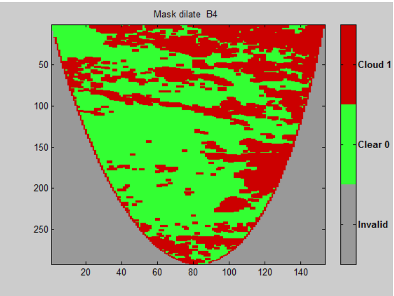

One image of final mask and its application on the NIR TOA reflectance

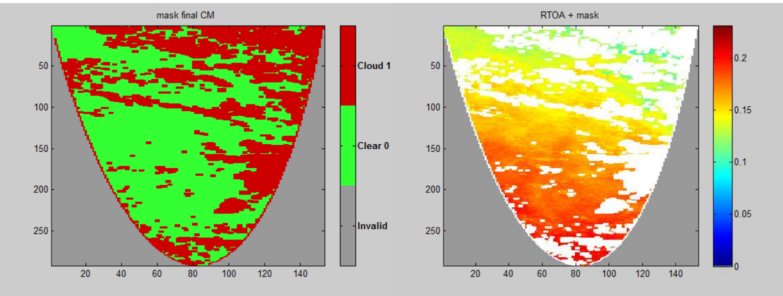

4.1.1.3 PARASOL cloud detection

The algorithm has been changed in order to take advantage of the directional information. As PARASOL provides the TOA reflectance for 16 directions, including sunglint and far from sunglint, the idea is to check that pixels acquired at the maximum of sunglint have a very low TOA NIR reflectance outside the sunglint.

The following figures represent the variability of the TOA reflectance for pixels acquired in the sunglint area where there are clouds, (Figure 58-a) and without clouds (Figure 58-b). Where there are no clouds and far from the specular conditions, the TOA reflectance is low (less than 5 %), whereas it is higher (more than 30 %) when clouds are present.

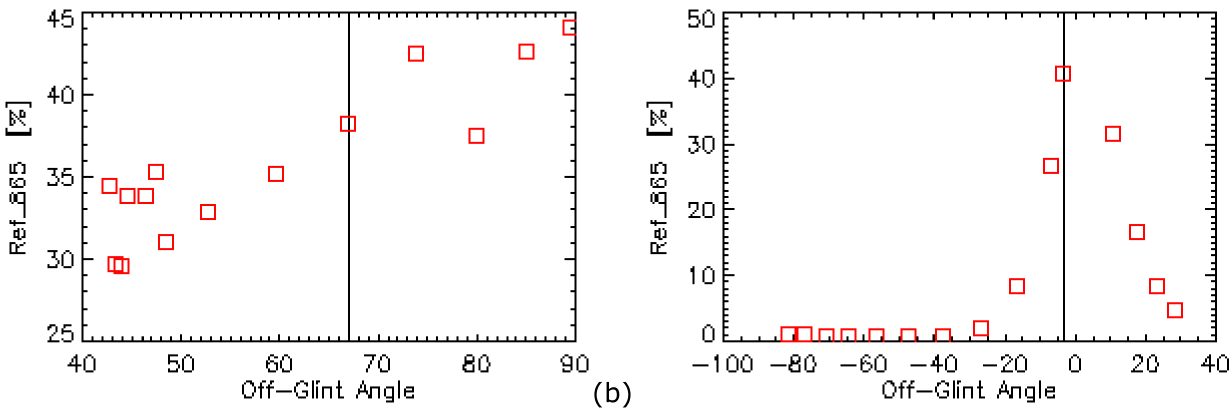

(a) (b)

Figure 58: TOA reflectance plotted as a function of the glint angle. Vertical black line is the exact specular direction.

The benefits of this detection are represented on the two following figures. In these figures, all TOA reflectances acquired in PARASOL NIR channel are plot as a function of the glint angle.

When the algorithm is applied only based on the level of the NIR reflectance acquired in the sunglint, the pixels detected as clouds are represented in blue, where the clear pixels are represented in red. When the second tests is added (Figure 59-b, the color code is inverted), we can see that in the sunglint region, some red points appear indicating new identified clouds.

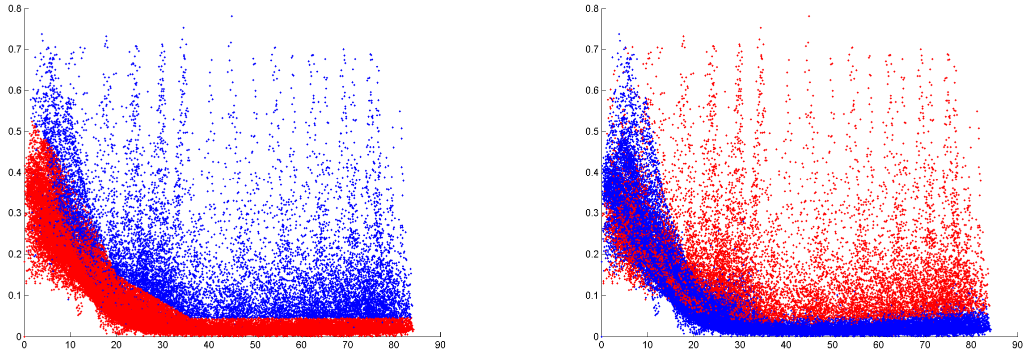

(a) (b)

Figure 59: Impact of directional information in the cloud detection algorithm

The processing is the same inside sunglint areas or outside sunglint areas, only specific thresholds have been set to detect cloud over sunglint.

Tests and Thresholds are reported in the table below.

Table 9: Overview of tests and Thresholds

Tests	Detect as cloud if	Threshold s	Thresholds for Sunglint path
Select VALID pixels in VIS and NIR			
Modified test on NIR reflectance	for pixels located in the sunglint area: $\rho(\theta r>36)$ > T1 for pixels located in the sunglint	0.045	T1 estimated as a function of θ_r (see Figure 54)
Test on NIR/VIS ratio	ρNIR/ ρVIS >T2	0.85	1.025
Spatial coherence	For a window of 3x3 pixels σ > T5_sdt OR abs(ρ-ρ mean) > T5_avg	T5_sdt = 0.01 T5_avg=0.01	T5_sdt = 0.015 T5_avg=0.015
Dilatation of cloud mask	Not applied on PARASOL		

4.1.1.4 AATSR cloud detection

The algorithm has been changed and is based on MODIS ATBD. Additional thresholds have been implemented. It used the NIR and VIS reflectance, and the temperature at 11 µm.

The processing is the same inside sunglint areas or outside sunglint areas, only specific thresholds have been set to detect cloud over sunglint.

Tests and Thresholds are reported in the table below.

Table 10: Overview of tests and Thresholds

Tests	Detect as cloud if	Threshold s	Thresholds for Sunglint path
Select VALID pixels in VIS and NIR			
Test on NIR reflectance	ρ > T1	0.045	T1 estimated as a function of θ_r (see Figure 54)
Test on NIR/VIS ratio	ρNIR/ ρVIS >T2	0.85	1.025
Test on BT 12 µm	TB < T4	273 K	273 K
Spatial coherence	For a window of 3x3 pixels σ > T5_sdt OR abs(ρ-ρ mean) > T5_avg	T5_sdt = 0.01 T5_avg=0.01	T5_sdt = 0.015 T5_avg=0.015
Dilatation of cloud mask		1 pixel	1 pixel

4.1.1.5 ATSR-2 cloud detection

Tests are identical to AASTR.

4.1.2 Over Land: Desert site

Libya 4 site is a desert site, which is bright and slightly heterogeneous in its south west part due to dunes which highlights spatial structures oriented NE-SW. This characteristic involves some variability in the surface reflectance over this large site (100 x 100 km) that could reach 10 % between the maximum and the minimum of the TOA reflectance measured by the satellite.

For the branch "LAND", the same philosophy that has been implemented for the cloud detection over the ocean site is applied. A set of tests based on thresholds is used to fill a cloud mask, and the final cloud mask is the product of all cloud masks. The final mask is dilated to avoid cloud border effects.

However, for this site, the algorithm has been redesigned to account for the radiometric knowledge of the area. Indeed, from the large time series of data acquired over the site, statistics have been performed to quantify spatially and temporally the annual variability of the

TOA reflectance. Using a dataset of data selected manually from data acquired under clear conditions, a climatology of TOA NIR MODIS reflectance has been built to be used as a reference map, providing the mean, the standard deviation of the reflectance, the minimum and the maximum on 1 year of data, and discard in a safe way cloudy acquisitions.

These maps are represented in the figures below. We can see that in this channel, the mean TOA reflectance is around 0.57, but fall to 0.50-0.53 (areas colored in blue) in 20% of the site. On the other site, the standard deviation is more homogeneous. A peak higher than 4 % is observed in the south of the site, indicating some changes in the TOA reflectance with time. This change could be related to stronger BDRF effects at this location or surface changes. The difference between the maximum and the minimum reflects the BRDF variability with the season.

This variability indicates clearly that an algorithm that uses this spatial and temporal information will better identify the cloud than an algorithm that will use a constant threshold for the scene.

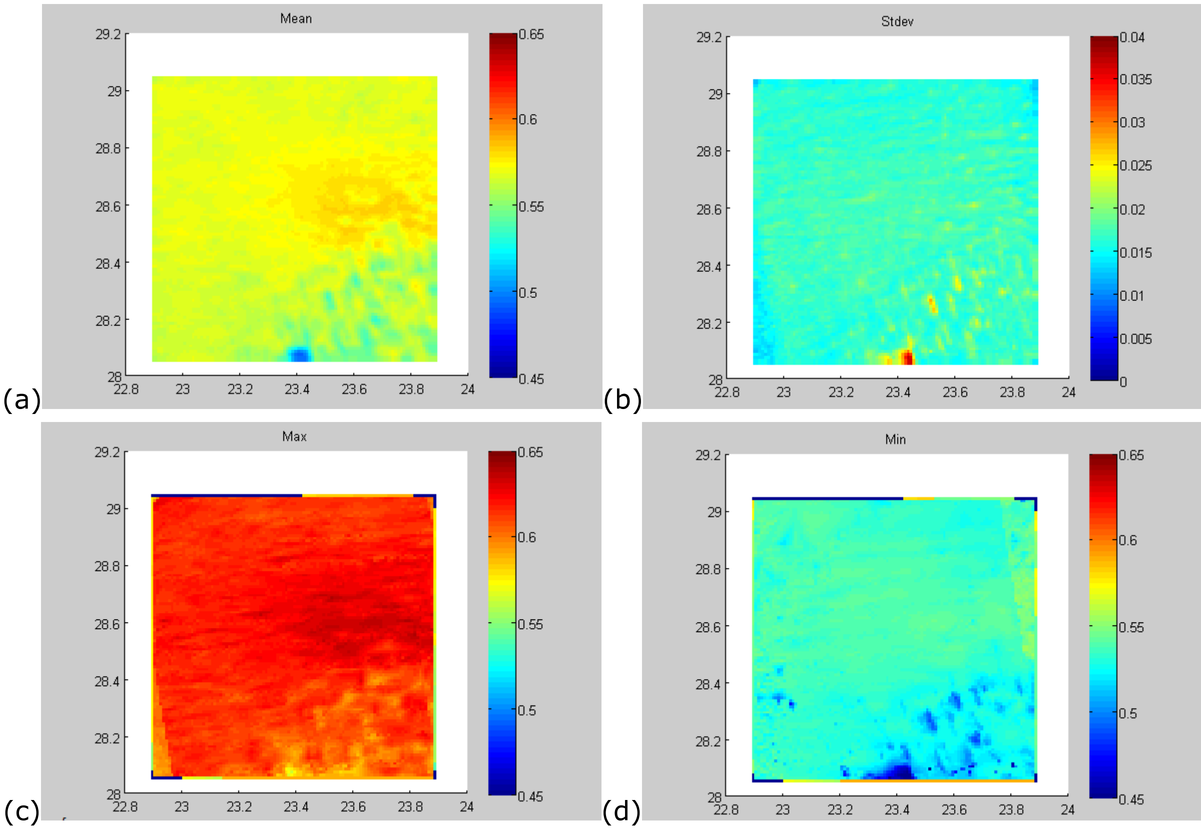

Figure 60: NIR TOA reflectance variability based on one year of clear acquisitions. (a) Mean, (b) Standard deviation, (c) Maximum, (d) Minimum.

Additional tests have been added to account for spectral information provided by cirrus or SWIR bands.

1) When the cirrus band is available, a simple threshold allows to discard the pixels for which the reflectance at 1.38 µm is high. The analysis has been performed on the global dataset of clear acquisitions selected to build the climatology. Figure 61 allows to identify two dates for which cirrus are present on the acquisitions. A threshold set to 1.5 % is implemented to remove these contaminated data.

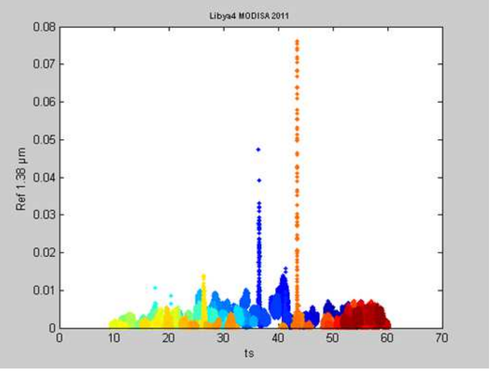

Figure 61: Cirrus reflectance plotted as a function of solar zenith angle

2) The ratio of SWIR/BLUE band is very sensitive to bright cloud and cloud shadow that could not be detected using the NIR TOA reflectance only. If the ratio is higher than the mean of the ratio of the acquisition +/- σ, the pixel is declared cloudy.

(a) (b) (c)

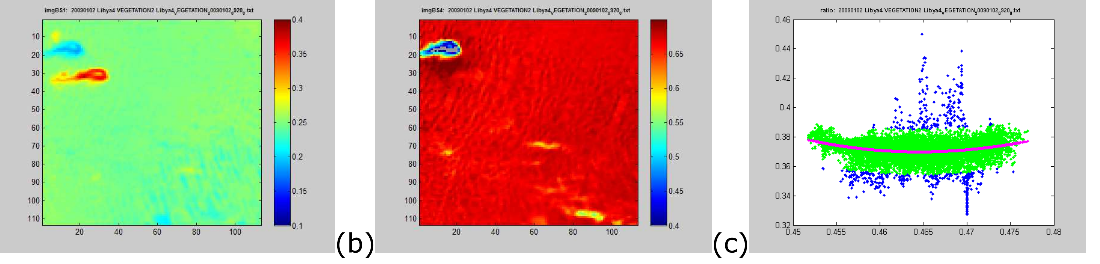

Figure 62: Usage of SWIR/BLUE test for VEGETATION. (a) BS1, (2) SWIR, (c) The mean ratio is represented in pink color as a function of phase angle. Cloudy and clear pixels are in blue and green color respectively.

The algorithm using the bright tests such as they are defined in the GLOBCARBON branch (MERIS, POLDER) are completely removed, and are based only on the algorithm that uses the NIR climatology.

The other algorithms are kept as they are, except that the test using the climatology is considered as an additional test.

Tests and Thresholds implemented are reported in the table below.

Table 11: Overview of tests and Thresholds

Tests	Detect as cloud if	Threshold s
Select VALID pixels in VIS and NIR		
Test on NIR TOA reflectance map	ρ > T1 + 2 * σ & ρ < T1 - 2 * σ	T1= TOA reflectance mean map σ = TOA reflectance standard deviation map
Test on Cirrus (if cirrus band is available)	ρ > T3	T3=0.015

Test on SWIR/BLUE band ratio	$\dfrac{\rho_{SWIR}^{TOA}}{\rho_{BLUE}^{TOA}}_{est} = f(\xi)$ $\dfrac{\rho_{SWIR}^{TOA}}{\rho_{BLUE}^{TOA}} > \dfrac{\rho_{SWIR}^{TOA}}{\rho_{BLUE}^{TOA}}_{est} + 2\sigma$ or $\dfrac{\rho_{SWIR}^{TOA}}{\rho_{BLUE}^{TOA}} < \dfrac{\rho_{SWIR}^{TOA}}{\rho_{BLUE}^{TOA}}_{est} - 2\sigma$	
Dilatation of cloud mask		1 pixel

4.1.2.1 MODIS cloud detection

Acquisition: 24/05/2008

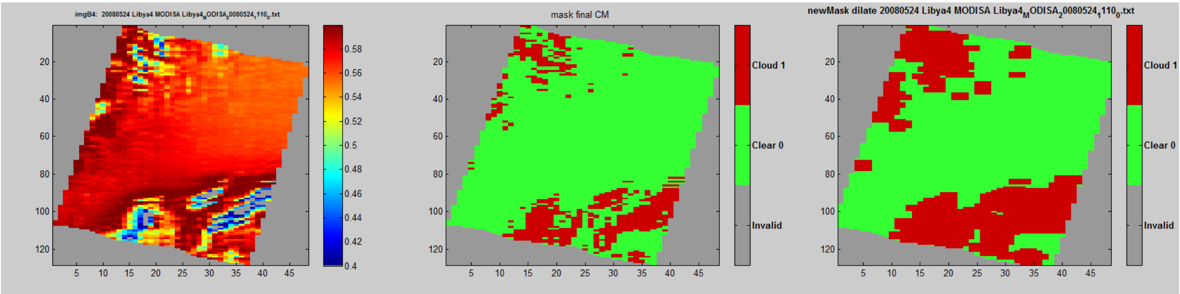

Figure 63: NIR TOA reflectance, cloud mask, dilated cloud mask

4.1.2.2 MERIS cloud detection

Acquisition: 14/05/2008

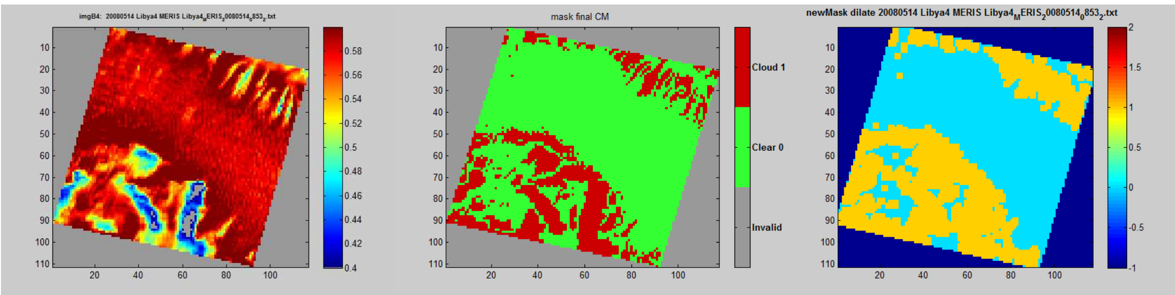

Figure 64: NIR TOA reflectance, cloud mask, dilated cloud mask

4.1.2.3 VEGETATION cloud detection

Acquisition: 24/04/2008

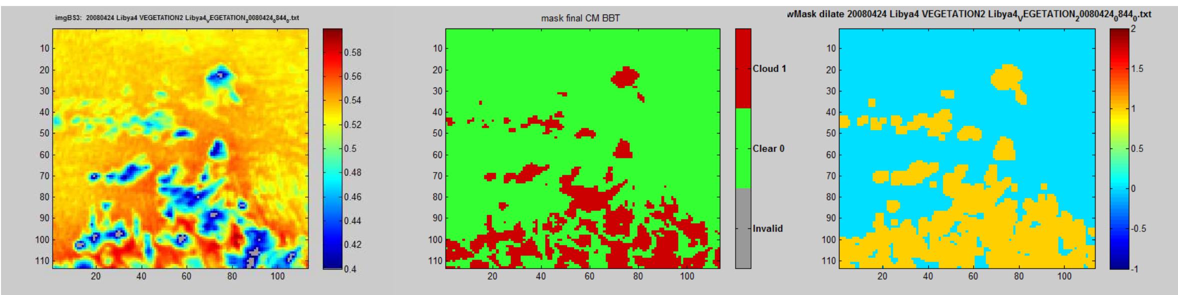

Figure 65: NIR TOA reflectance, cloud mask, dilated cloud mask

4.1.2.4 AATSR cloud detection

Acquisition: 12/09/2012

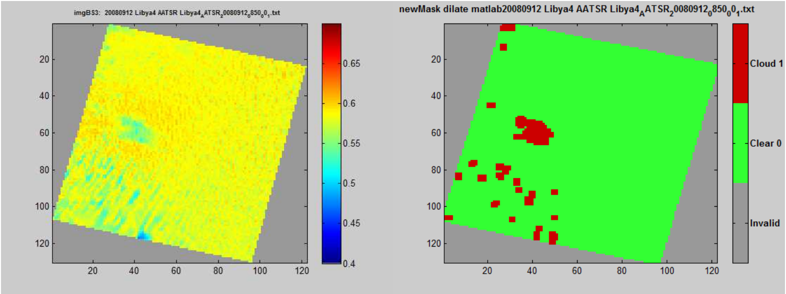

Figure 66: NIR TOA reflectance, cloud mask, dilated cloud mask

4.1.2.5 ATSR-2 cloud detection

Acquisition: 03/02/2003

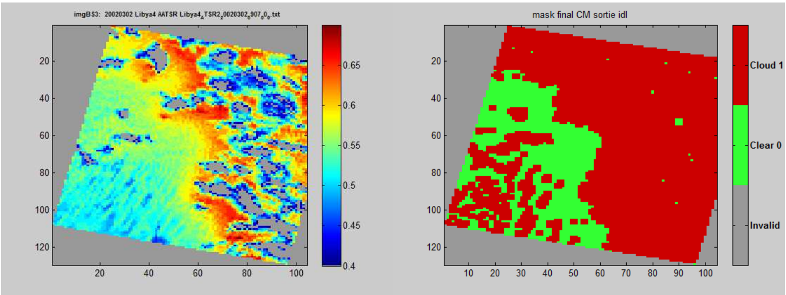

Figure 67: NIR TOA reflectance, cloud mask, dilated cloud mask

4.1.2.6 PARASOL cloud detection

Acquisition: 21/05/2011
Masks are displayed for the 14 directions available.

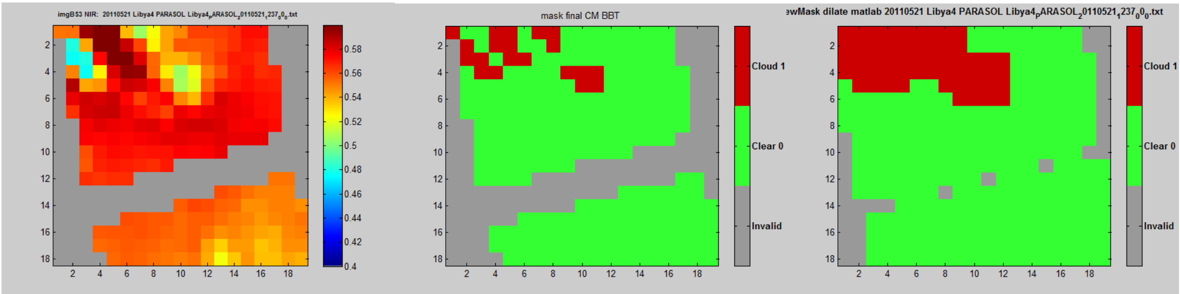

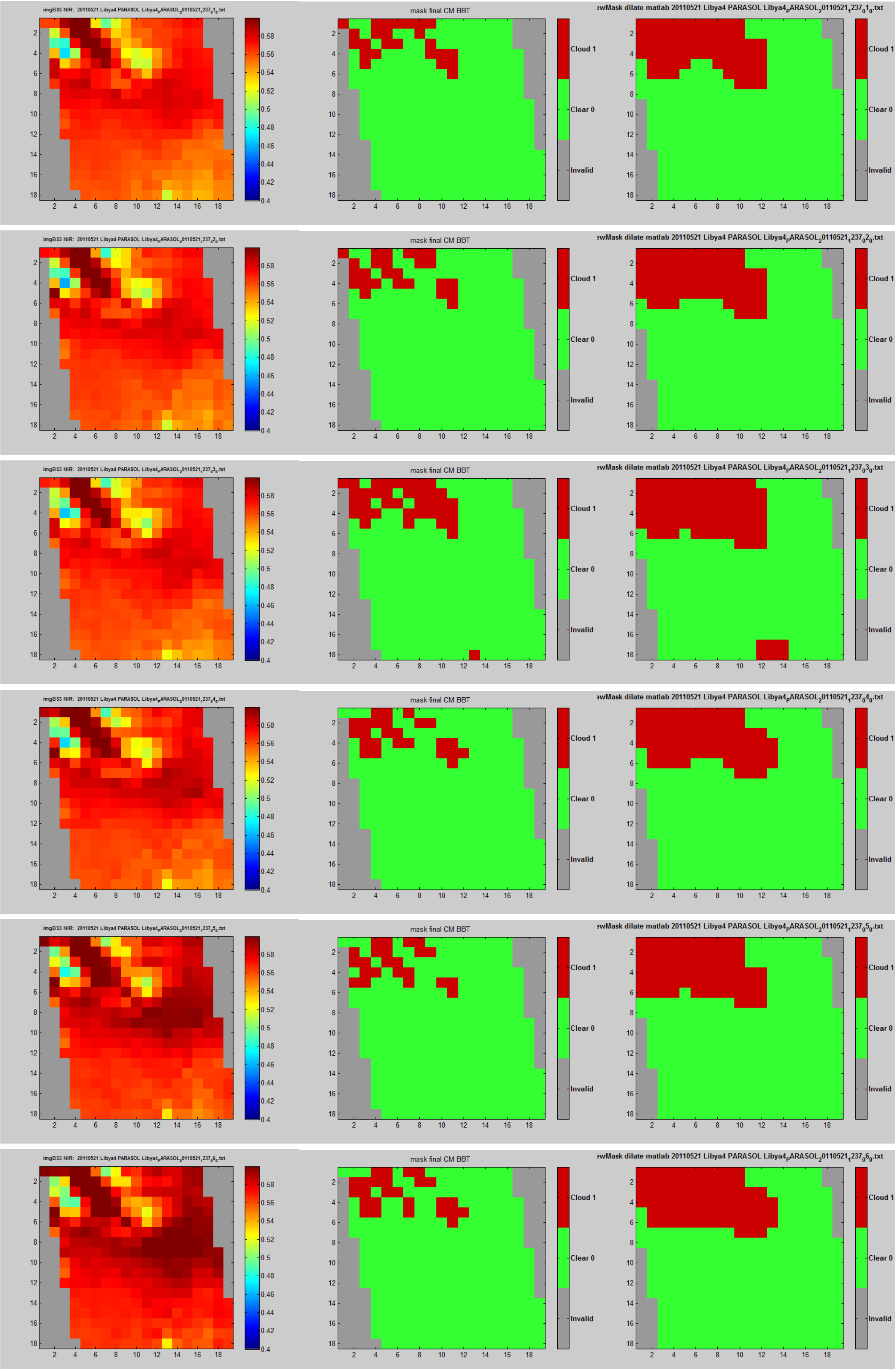
mask final CM BBT
Cloud 1
Clear 0
Invalid

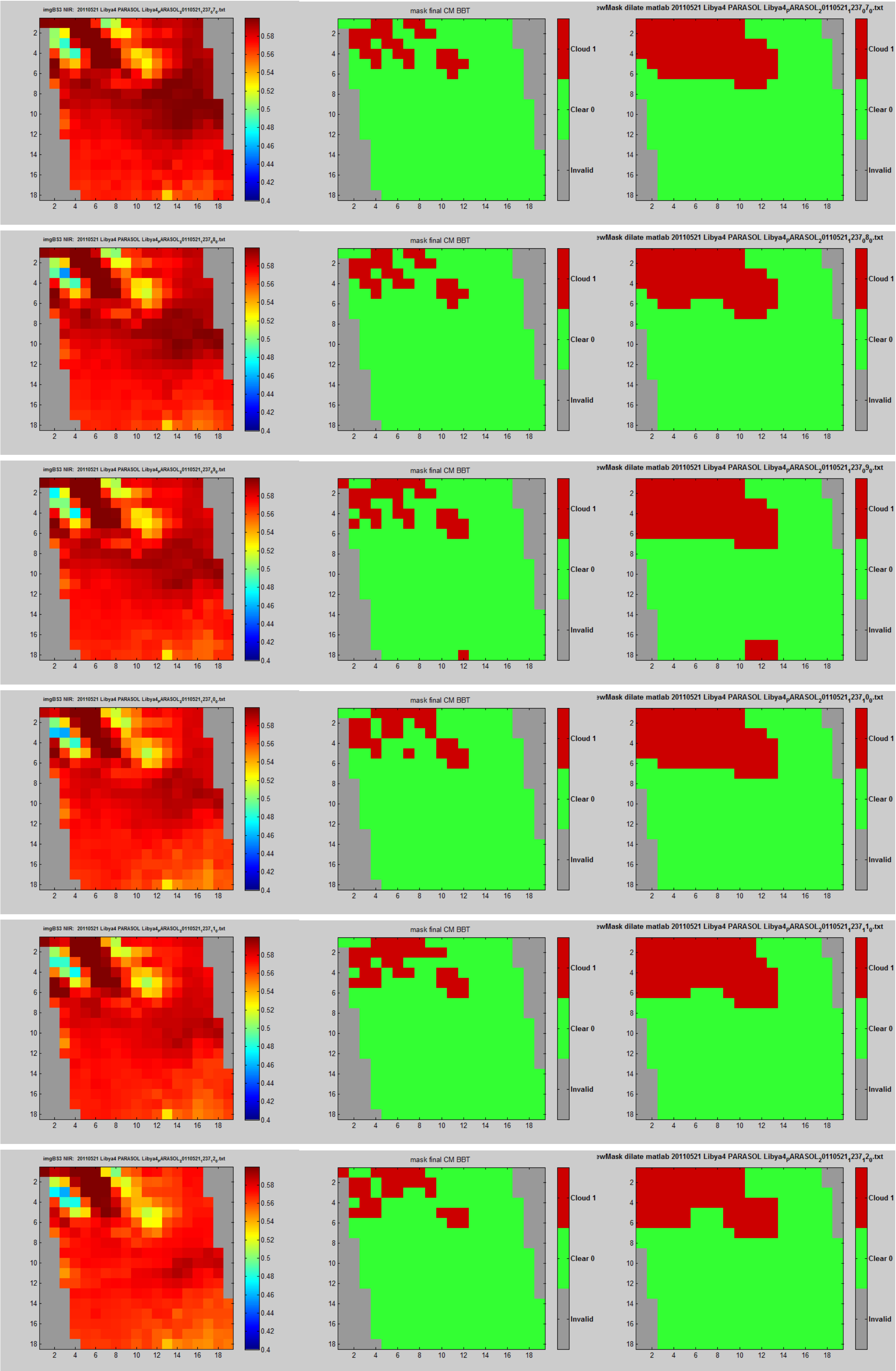
mask final CM BBT
Cloud 1
Clear 0
Invalid

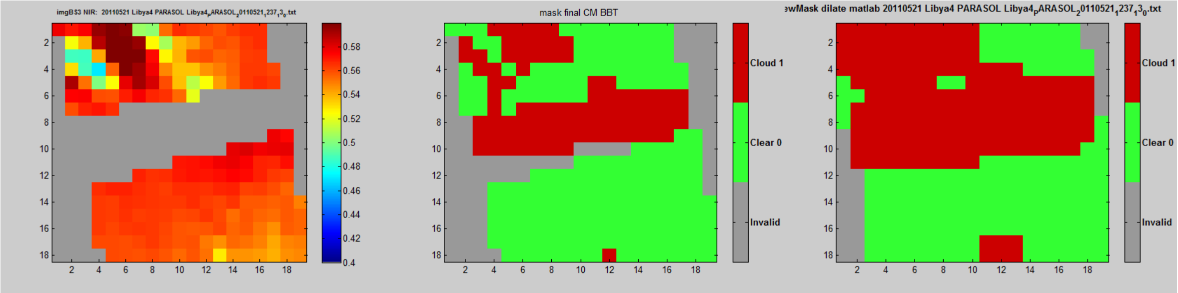

Figure 68: NIR TOA reflectance, cloud mask, dilated cloud mask. From top to bottom, direction 1 to 14.

4.2 Results

4.2.1 Over ocean

Then analysis is performed in two steps. First, the temporal profiles of TOA reflectances are plotted as a function of time, as it has been made in the analysis of the reference data. Second, the cloud mask are examined for each acquisition/each sensor in order to detect visually if there are still over/underestimation, if the cloud boarders have been well masked by the cloud dilation step, and finally, assess the spatial structure of the clear pixels that will be used as input of the calibration processes.

For ocean sites, the analysis allows to flag the data acquired in sunglint conditions, meaning that the reflected sun angle is lower than 36 degrees. The mean reflected sun angle for the SIO and SPG site reaches rarely the values for which the data will be selected for sensor radiometry estimation that is lower than 7 degrees (equivalent to the wave angle of 4 degrees). This means that a second dataset dedicated to sensor radiometry monitoring using sunglint target has been extracted on the available acquisitions. This data is extracted from L1b available in the input database.

The two figures below explain how the data are extracted. The site, here SIO, is represented by a red square inside the image, NIR reflectance. The image on the right is an image of θn. Pixels with a θn lower than 4 degrees are masked in brown. So, data over the site are extracted as regular data of DIMITRI. And data inside the semi ellipse are extracted for sunglint calibration purposes.

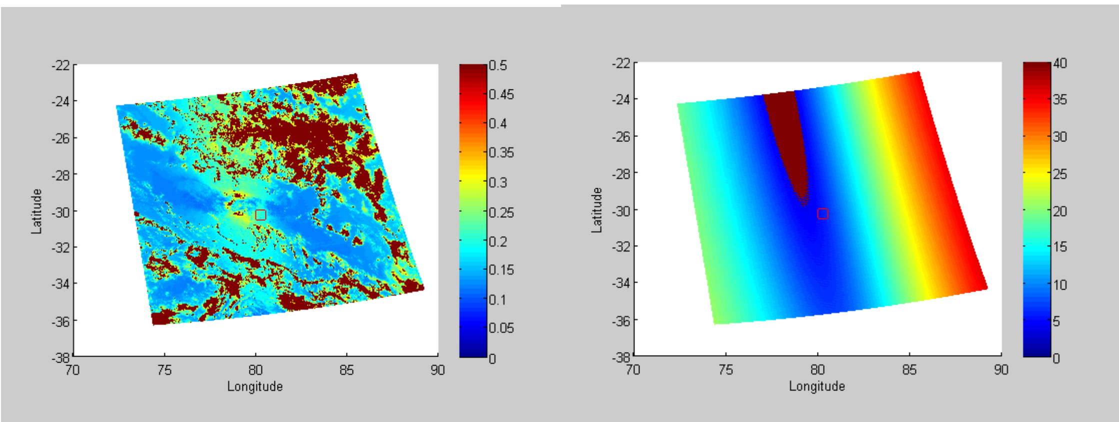

Figure 69: SIO site location on a MODIS acquisition. NIR reflectance on the left, Sun reflected angle on the right.

As it is observed in the following figure, cloud percentage is very coherent with the level of TOA reflectance.

4.2.2 MODIS

4.2.2.1 SIO

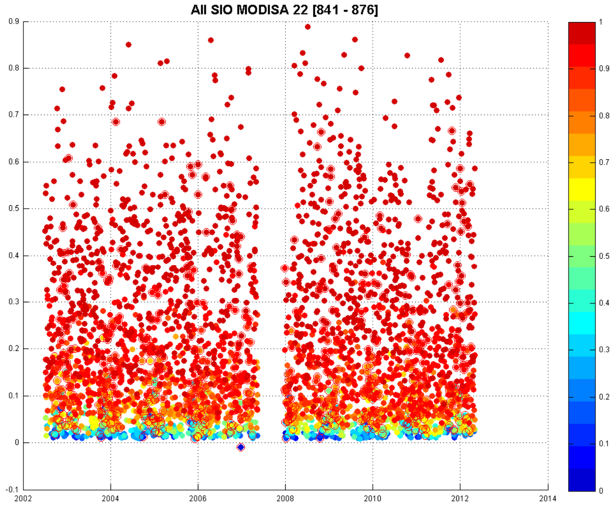

Figure 70: NIR TOA reflectance versus acquisition time. Cloud coverage level is indicated with colortable. Red circle indicate that data has been acquired on sunglint area.

4.2.2.2 SPG

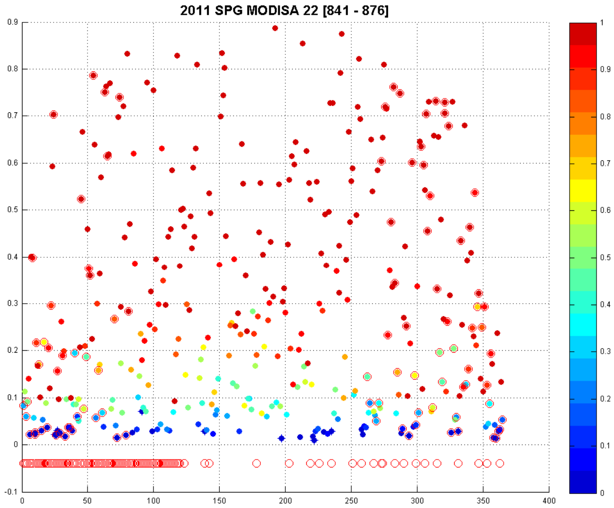

Figure 71: NIR TOA reflectance versus acquisition time. Cloud coverage level is indicated with colortable. Red circle indicate that data has been acquired on sunglint area.

4.2.2.3 Boussole

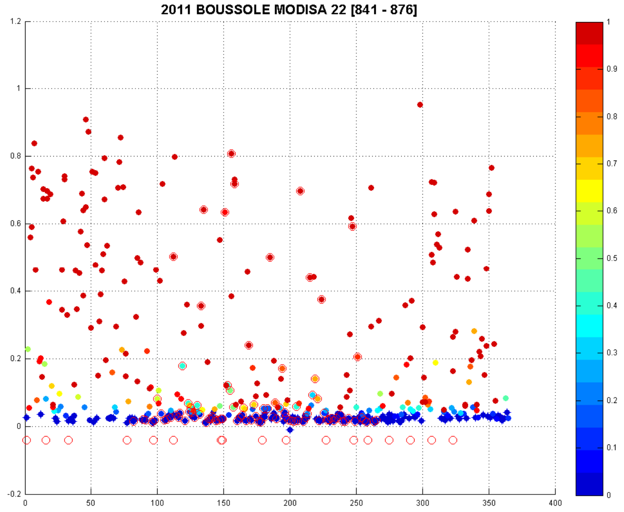

Figure 72: NIR TOA reflectance versus acquisition time. Cloud coverage level is indicated with colortable. Red circle indicate that data has been acquired on sunglint area.

4.2.2.4 Libya4

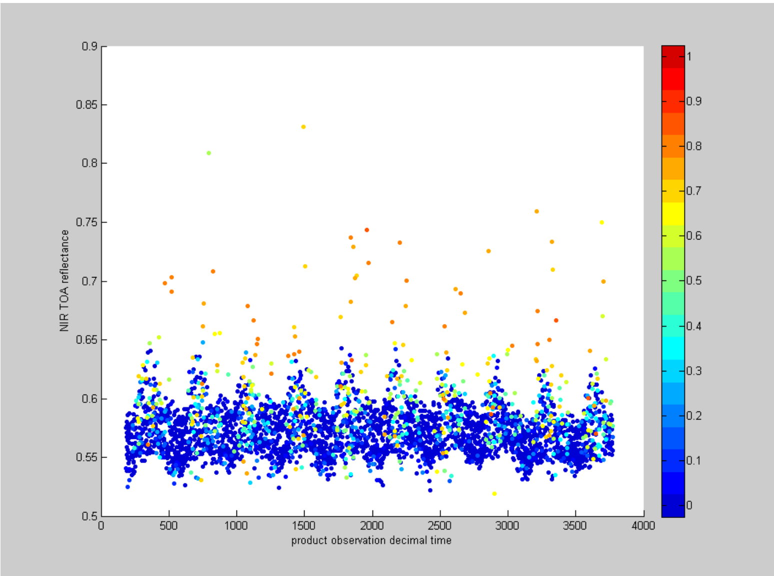

Figure 73: NIR TOA reflectance versus acquisition time. Cloud coverage level is indicated with colortable.

4.2.3 MERIS

4.2.3.1 SIO

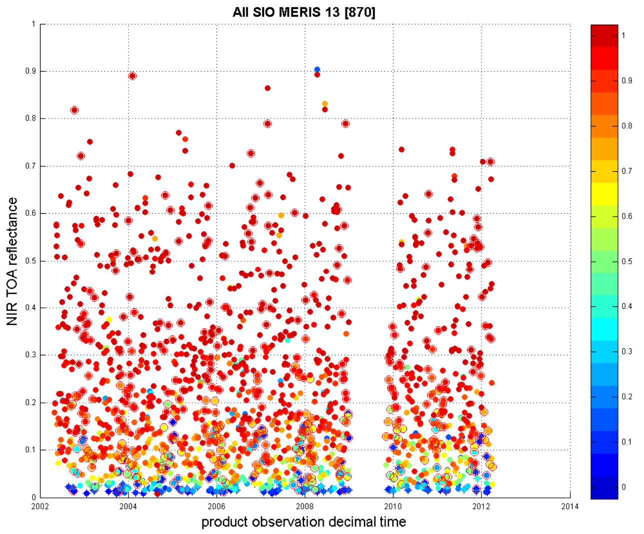

Figure 74: NIR TOA reflectance versus acquisition time. Cloud coverage level is indicated with colortable.

4.2.3.2 Libya4

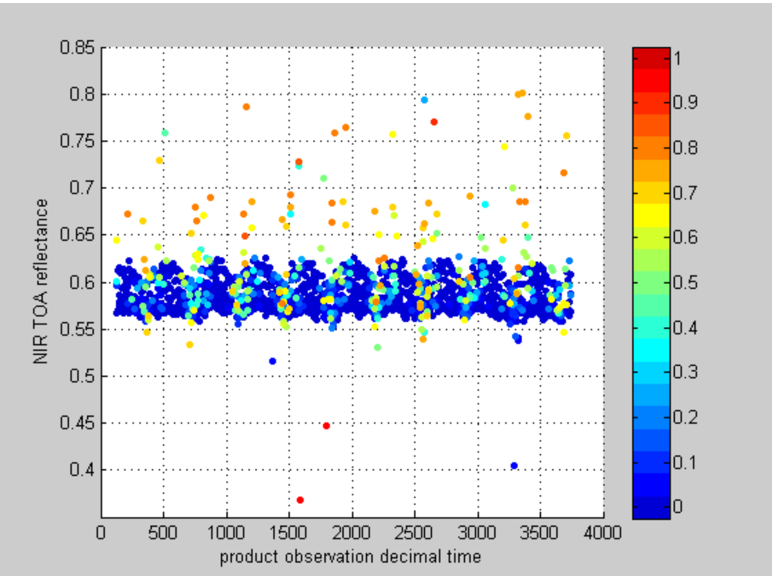

Figure 75: NIR TOA reflectance versus acquisition time. Cloud coverage level is indicated with colortable.

4.2.4 AATSR

4.2.4.1 SIO

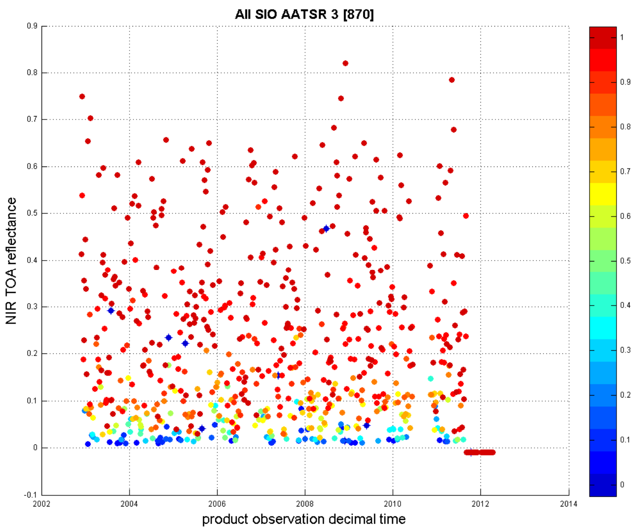

Figure 76: NIR TOA reflectance versus acquisition time. Cloud coverage level is indicated with colortable.

4.2.4.2 Libya4

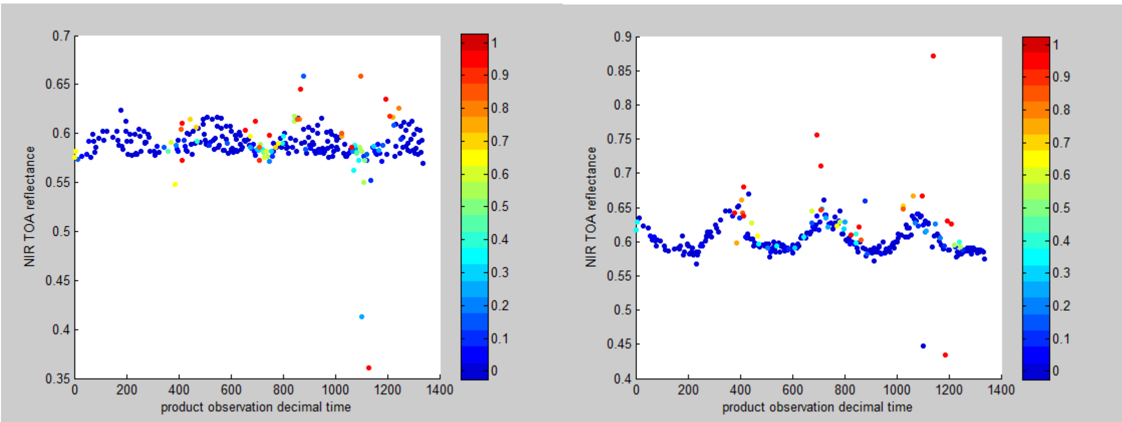

Figure 77: NIR TOA reflectance versus acquisition time. Cloud coverage level is indicated with colortable.

4.2.5 PARASOL

4.2.5.1 SIO

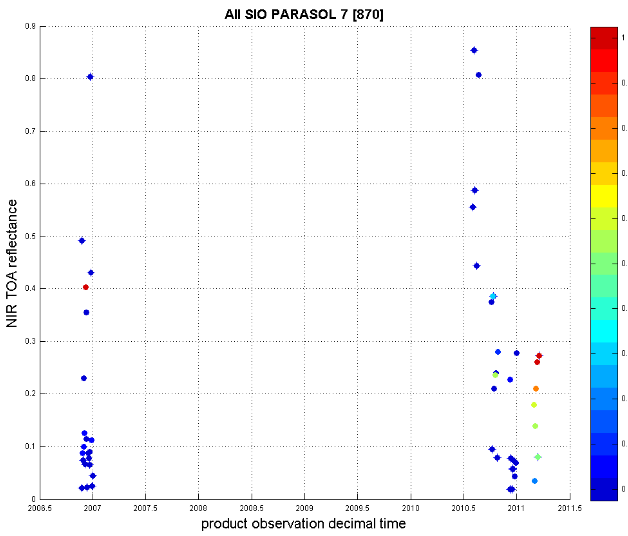

Figure 78: NIR TOA reflectance versus acquisition time. Cloud coverage level is indicated with colortable.

4.2.5.2 Libya4

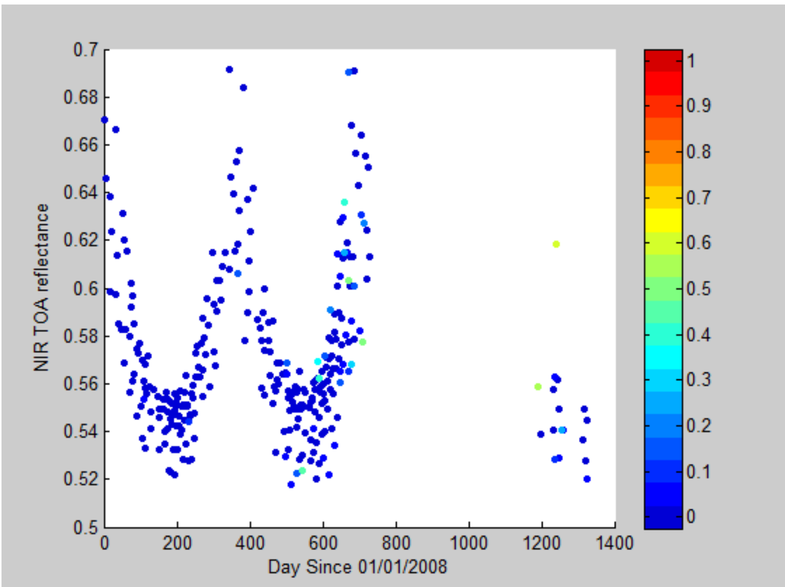

Figure 79: NIR TOA reflectance versus acquisition time. Cloud coverage level is indicated with colortable.

4.2.6 VEGETATION

4.2.6.1 SIO

N/A

4.2.6.2 Libya4

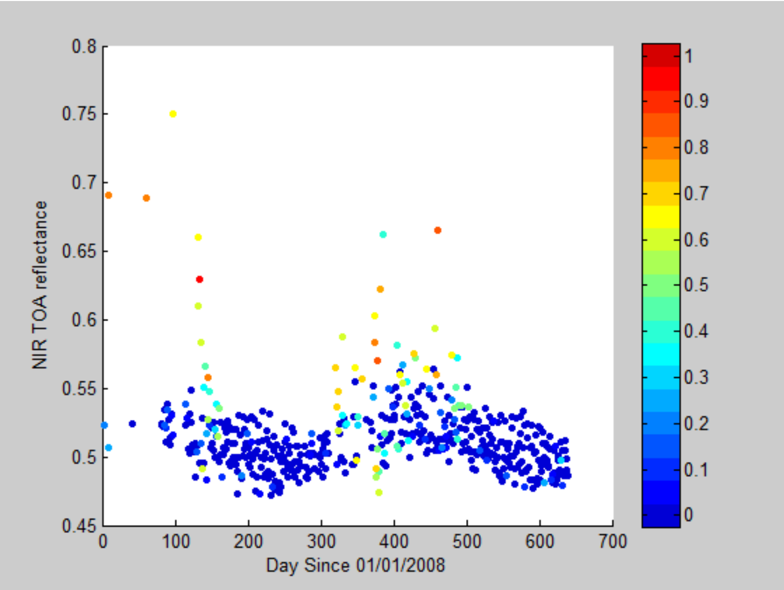

Figure 80: NIR TOA reflectance versus acquisition time. Cloud coverage level is indicated with colortable.

4.2.7 ATSR2

4.2.7.1 SIO

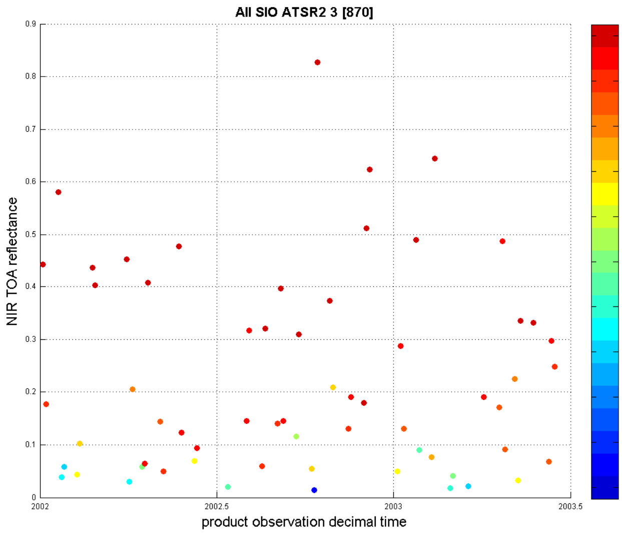

Figure 81: NIR TOA reflectance versus acquisition time. Cloud coverage level is indicated with colortable.

4.2.7.2 Libya4

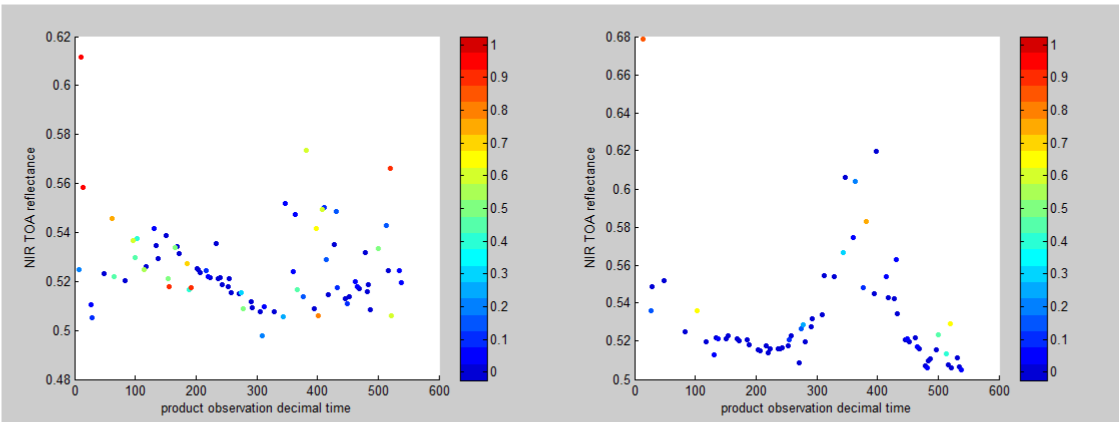

Figure 82: NIR TOA reflectance versus acquisition time. Cloud coverage level is indicated with colortable. (Nadir view on the left and forward view on the rigth)

- End of the document -